

High Vertical Shear and Dissipation in Equatorial Topographic Wakes

KAUSHIK SRINIVASAN,^a JAMES C. MCWILLIAMS,^a AND ARJUN JAGANNATHAN^a

^aDepartment of Atmospheric and Oceanic Sciences, University of California, Los Angeles, Los Angeles, California

(Manuscript received 30 May 2020, in final form 28 November 2020)

ABSTRACT: Submesoscale coherent vortices (SCVs) are a ubiquitous feature of topographic wakes in the extratropical oceans. Recent studies demonstrate a mechanism wherein high-vorticity bottom boundary layers (BBLs) on the slopes of the topography separate (forming shear layers), undergo instabilities, and subsequently merge in the horizontal and align in the vertical to form vertically coherent, columnar SCVs (i.e., with low vertical shear). Background rotation is critical to the vertical alignment of unstable vortical filaments into coherent SCVs. In the tropics, however, the weakening of rotation prevents this alignment. Employing an idealized framework of steady barotropic flow past an isolated seamount in a background of constant stratification N and rotation rate f , we examine the wake structure for a range of f values spanning values from the poles to the tropics. We find a systematic increase in the interior vertical shear with decreasing f that manifests as a highly layered wake structure consisting of vertically thin, “pancake” SCVs possessing a high vertical shear. A monotonic increase in the wake energy dissipation rate is concomitantly observed with decreasing f . By examining the evolution equations for the vertical shear and vertical enstrophy, we find that the interior shear generation is an advective process, with the location of peak shear generation approximately collocated with maximum energy dissipation. This leads to the inference that high-wake dissipation in tropical topographic wakes is caused by parameterized shear instabilities induced by interior advective generation of vertical shear in the near wake region.

KEYWORDS: Ocean; Tropics; Bottom currents; Boundary currents; Eddies; Topographic effects

1. Introduction


Geostrophic oceanic currents interact with topography along their path, generating high-vorticity bottom boundary layers (BBLs) on the slopes of the topography (Molemaker et al. 2015; Gula et al. 2015b, 2016). The BBLs on the slopes possess high values of vorticity and vertical shear, which on separation can be injected into the fluid in the form of separated shear layers (Molemaker et al. 2015). These separated shear layers are subject to horizontal inflection point instabilities, leading to the formation of vortical filaments that have small horizontal and vertical length scales (relative to the size of the seamount itself) (Srinivasan et al. 2019, hereafter S19). Away from the tropics, these vortical filaments subsequently merge rapidly in the horizontal and align in the vertical to form horizontally and vertically coherent submesoscale coherent vortices (SCVs) (McWilliams 1985; Molemaker et al. 2015; S19). These bottom drag-mediated SCVs are ubiquitous in global oceans, in particular in topographic wakes that lie along the path of prominent eastern and western boundary currents (D’Asaro 1988; Gula et al. 2015b, 2016; Vic et al. 2015; Molemaker et al. 2015; Srinivasan et al. 2017; Zhang et al. 2020), the North Equatorial Current and Countercurrent (Wijesekera et al. 2020; St. Laurent et al. 2019; Simmons et al. 2019; Johnston et al. 2019), and the Antarctic Circumpolar Current (Rosso et al. 2014). While other common outcomes of

flow–topographic interactions in the ocean are possible, in particular resulting in the generation of lee waves (Nikurashin et al. 2014; Wright et al. 2014; Perfect et al. 2020b), hydraulic jumps (Epifanio and Durran 2002), and locally enhanced baroclinicity (Bischoff and Thompson 2014; Abernathy and Cessi 2014) (and consequently baroclinic instability), the current study focuses on bottom drag-mediated effects only. The precise nature of the interaction is governed by two nondimensional parameters: the bulk Rossby number, Ro_L , and the steepness parameter, $s = Fr_v^{-1}$, where Fr_v is the vertical Froude number, defined as

$$Ro_L = \frac{U}{fL}, \quad s = \frac{Nh}{U}. \quad (1)$$

Here U is the flow speed upstream of the topography, f is the local Coriolis parameter, N the associated buoyancy frequency of the incoming stratified flow, and L and h are the horizontal and vertical length scales that characterize the topography. Regimes of strong bottom-drag mediated flow–topography interaction, as opposed to the other mechanisms stated above, require that the steepness parameter $s \gg 1$ (Perfect et al. 2020b), typical of eastern (Molemaker et al. 2015) and western boundary currents (Gula et al. 2015b, 2016; Vic et al. 2015) in the strongly stratified upper thermocline.

S19 employ the exact idealized flow configuration used here to examine the generation of wake SCVs, for $Ro_L \ll 1$ (typical of midlatitudes and large-scale, $L \sim O(10)$ km, topographic features) and steepness parameters in the range $0 < s < 47$. S19 further find that a nondimensional height, $\hat{h} = sRo_L$ (equivalently $\hat{h} = h/h_T$, where $h_T = fL/N$ is the Taylor height) is the relevant parameter that describes low- Ro_L SCV generation, in particular finding that robust SCV regimes require $\hat{h} > 1$, as

 Denotes content that is immediately available upon publication as open access.

Corresponding author: Kaushik Srinivasan, kaushiks@atmos.ucla.edu

DOI: 10.1175/JPO-D-20-0119.1

© 2021 American Meteorological Society. For information regarding reuse of this content and general copyright information, consult the AMS Copyright Policy (www.ametsoc.org/PUBSReuseLicenses).

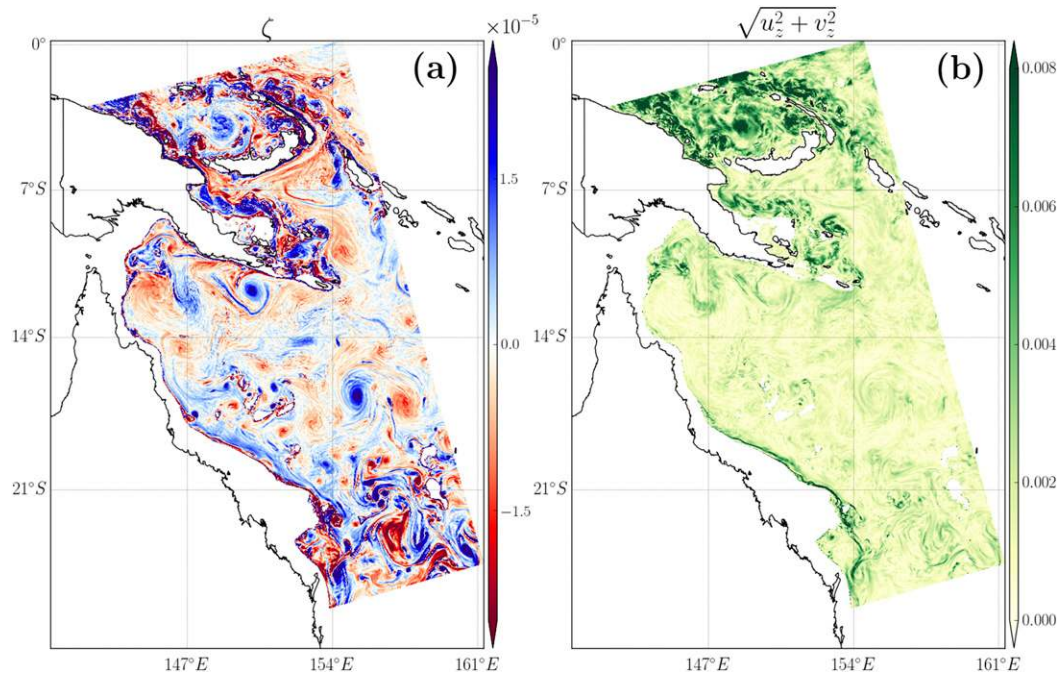


FIG. 1. A single snapshot of (a) vertical vorticity (s^{-1}) and (b) vertical shear (s^{-1}) from a $\Delta x = 1.2$ km ROMS process study (Srinivasan et al. 2017) in the southwest Pacific at a depth of 200 m.

found in upper-ocean thermocline currents and topography along their path. A detailed discussion of the life cycle of wake SCV generation, starting from the structure of the BBLs on the slopes of the topography to their separation, instability, and merger in the horizontal and alignment, and the associated dynamics, can be found in that study. In particular, they find that the BBLs (and associated near-wake shear layers) on slopes have high horizontal and vertical shears that are related by

$$v_x = v_z \theta_b, \quad (2)$$

where v is the local along-slope velocity, $\theta_b \ll 1$ is the local topographic slope, and x is the cross-slope direction. Furthermore, the far-wake SCVs were found to have an aspect ratio,

$$\frac{L_x}{L_z} \sim \sqrt{\frac{f}{N}}, \quad (3)$$

where L_x and L_z are characteristic horizontal and vertical scales of the wake SCVs. Note that the scaling in (3) departs from quasigeostrophic scaling $L_x/L_z \sim f/N$, a consequence of the $\text{Ro}_\zeta \sim 1$ ($\text{Ro}_\zeta = \zeta/f$, where $\zeta = v_x - u_y$) values typical of SCVs; high values of Ro_ζ mean that the vortices are no longer geostrophically balanced but gradient-wind balanced.

This study, which can be considered a natural extension of the issues examined by S19 (focusing on flow regimes with $\text{Ro}_L \ll 1$), aims to understand the structure and dynamics of wakes in the limit of $f \rightarrow 0$ (so Ro_L is no longer a small number), i.e., the tropical oceans. The motivation of examining this parameter regime stems from the tropical wake structure observed in realistic, high-resolution ROMS simulations in and

around the Solomon Sea in the southwest Pacific (Srinivasan et al. 2017) and recent observations in the same region (Alberty et al. 2017), and in the wake of the Palau archipelago, north of the equator (MacKinnon et al. 2019). Figure 1a shows a snapshot of the vorticity at a depth of 300 m from the ocean surface in the southwest Pacific. The waters in the region are fed from the westward South Equatorial Current (SEC) that bifurcates to the north and south around 18°S . The northward (equatorward) boundary current, which has a subsurface maximum (between 100 and 300 m) flows along the Australian coast through the coast of Papua New Guinea and into the Solomon Sea. Complex topography along the path of the western boundary current lead to strongly vortical topographic wakes, although the wake structure is highly dependent on latitude (Fig. 1a): large coherent eddies away from the equator and a mix of incoherent wakes and large vortices with small-scale features near the equator. Perhaps more striking and easier to discern is the vertical shear $\sqrt{u_z^2 + v_z^2}$ (Fig. 1b) that shows a sharp equatorward increase, especially north of 10° . In a parallel study (Srinivasan and McWilliams 2021, unpublished manuscript), we show that the tropical wakes in the region are also regions of strong mixing and dissipation. These results compare favorably with Alberty et al. (2017), who find high values of dissipation at the pycnocline depth (corresponding to the core of the subsurface boundary currents) in the Solomon Sea region that are not correlated with dissipation of internal tides.

In this study, we offer evidence for the hypothesis that the changes in the wake structure are a strong function of the f (equivalently Ro_L). In an idealized model setup, we demonstrate that with all other flow conditions held constant, simply

decreasing f (increasing Ro_L) from values found in the poles to those in the equator leads to highly sheared topographic wakes that are also regions of strong energy dissipation. A recent set of studies (Perfect et al. 2018, 2020a) employing the same idealized framework used here (and in S19) study the phenomenology and energetics of seamount wakes in (Ro_L, Fr_v) space. Perfect et al. (2020a), in particular, estimate empirical scaling laws for various components of the volume averaged eddy energy equation from model data. Here, we instead focus on the wake dynamics, in particular we identify the generation and dissipation sources of enstrophy and vertical shear in the wake to unravel the physical mechanisms of high dissipation values observed in the limit of $f \rightarrow 0$ (large Ro_L). Furthermore, we compare the results obtained here with a geostrophic to stratified turbulence transition, commonly studied in the paradigm of homogeneous turbulent studies (Waite and Bartello 2006; Vallgren et al. 2011; Deusebio et al. 2013), and highlight important differences in the two mechanisms.

Our manuscript is organized as follows: section 2 details the numerical model configuration and dynamical equations of enstrophy, vertical shear and eddy kinetic energy whose components we analyze. Section 3 examines the wake phenomenology, focusing on the observed enstrophy, vertical shear, energy, and integral scales as a function of downstream distance. Section 4 examines the various terms of dynamical equations of enstrophy, shear, and eddy kinetic energy to detail the generation and dissipation sources of each and connections between them. The subsequent discussion section compares the results in the present study with classical rotating, stratified turbulence and instability theories. This section also examines the validity of the hydrostatic primitive equations for the problem studied here. The final section summarizes our findings.

2. Methods

a. Idealized flow configuration

Because the idealized experimental setup mimics the one in S19, we direct the readers to that study for further details of the motivation and justification of the setup, and merely note the specifics of the configuration. The basic setup is a barotropic flow past a seamount in uniform background stratification N and Coriolis parameter f . The background velocity is set to $U = 0.1 \text{ m s}^{-1}$, which is in line with the largest values seen in the deep ocean bottom, except the Southern Ocean but small for eastern and western boundary currents that can have $O(1) \text{ m s}^{-1}$ currents on topographic slopes. The stratification, specified by the Brunt-Väisälä frequency, is fixed at $N = 6 \times 10^{-3} \text{ s}^{-1}$ typical of the oceanic thermocline and corresponding to the largest values found there. A range of Coriolis parameter values $1 \times 10^{-5} \text{ s}^{-1} < f < 1 \times 10^{-4} \text{ s}^{-1}$ corresponding to the latitude ranges $[5^\circ, 60^\circ]$ are considered, and the seamount shape is chosen to be Gaussian,

$$h_b(x, y) = h_s \exp[-(x^2 + y^2)/L^2], \quad (4)$$

where the seamount half-width, $L = 15 \text{ km}$, and height, $h_s = 800 \text{ m}$, are fixed in all the results shown here; f is therefore the only variable.

b. Nondimensionalization

We nondimensionalize space and time dimensions in the form

$$\hat{x} = x/L, \quad \hat{y} = y/L, \quad \hat{z} = z/h_T, \quad \hat{t} = Ut/L, \quad (5)$$

where the incoming background barotropic flow U is along the y direction. A key nondimensional parameter in S19 was the nondimensional height

$$\hat{h} = h_s N/fL = Ro_L s, \quad (6)$$

which is related to the Burger number for this problem, as $Bu = (Ro_L s)^2 = \hat{h}^2$, where Ro_L and s have been defined earlier in (1). The horizontal Froude number, commonly employed as the principle nondimensional parameter in stratified wake studies is

$$Fr_h = \frac{U}{NL}, \quad (7)$$

which also measures the importance of the nonhydrostatic terms in the vertical momentum equation (Schär 2002; Gill 2016). In all the cases examined in this manuscript, we have $Fr_h \ll 1$. Schär (2002) suggests that this means that the dynamics is predominantly hydrostatic. However, because the topographic wakes found here have strong horizontal and vertical shears that typically lead to three-dimensional instabilities, this conclusion is not straightforward and needs further justification as is offered in section 5 below. S19 also examined the role of the depth ratio

$$\gamma = h_s/D, \quad (8)$$

where D is the total water depth. They demonstrated that γ was only relevant when $\hat{h} \ll 1$, barring which the flow dependence on γ could be neglected. Because we always consider $\hat{h} \gg 1$ in this study, we do not subsequently reference γ in this study.

Thus the flow configuration can be completely described by three independent nondimensional parameters (Ro_L, Fr_v, α) , where $\alpha = h_s/L$ is the seamount aspect ratio; Fr_h and $\hat{h} = Ro_L/Fr_v$ can be derived from these quantities while the steepness parameter is just $s = 1/Fr_v$. In both this study and S19, $\alpha \ll 1$ given that oceanic topographic typically have shallow slopes (see S19 for a more detailed discussion on this front). In this study $\alpha \approx 0.03$ is fixed to the same value as S19. S19 further chose $Ro_L = 0.1$ varying $Fr_v \in [0.02, 1]$ (by varying $N \in [0.0005/s, 0.006/s]$), which leads to $\hat{h} \in [0.1, 4.7]$. Our starting point in this study is the $\hat{h} = 4.7$, $Fr_v = 0.02$ case from S19, because of the presence of robust, vertically coherent SCVs and a stratification value of $N = 0.006/s$ that is relevant to the upper-ocean currents. Then we fix this value of Fr_v and vary $Ro_L \in [0.05, 2]$ (corresponding to $\hat{h} \in [2.35, 94]$).

As is true for various rotating-stratified turbulent flow paradigms (Praud et al. 2006; Marino et al. 2013), the relative strength of rotation and stratification, N/f , is a key parameter, here captured by \hat{h} . S19 increase \hat{h} by increasing N , whereas here we do the same by decreasing f . The difference being that in the ocean, N has a maximum value of around 0.01 s^{-1}

limiting how large \hat{h} can be for fixed f . However, because f has no lower bound, arbitrarily large values of \hat{h} can occur moving equatorward.

c. Computational model

We employ ROMS, a primitive equation, split-explicit, hydrostatic, terrain-following σ -coordinate oceanic model (Shchepetkin and McWilliams 2003, 2005). Momentum advection is computed using a third-order upwind-biased scheme (Shchepetkin and McWilliams 2003, 2005) that is equivalent to a fourth-order central-difference scheme supplemented by a biharmonic diffusion operator whose hyper-viscosity depends both on local velocity u and the grid spacing Δx as

$$\nu = \frac{|u|\Delta x^3}{12}. \quad (9)$$

The turbulent bottom drag is parameterized as

$$\frac{\tau_b}{\rho_0} = \underbrace{[\kappa/\log(\Delta z_b/z_{ob})]^2}_{c_d} \|\mathbf{u}_b\| \mathbf{u}_b, \quad (10)$$

where ρ_0 is a reference density, \mathbf{u}_b is the velocity in the bottommost σ layer, $\kappa = 0.41$ is the von Kármán constant, Δz_b is the thickness of the bottommost σ layer, and $z_{ob} = 1$ cm is the roughness parameter. The BBL is parameterized through KPP (Large et al. 1994), using the variational formulation described in McWilliams et al. (2009). Vertical mixing is also added in the flow interior whenever the gradient Richardson number at a point in space falls below the threshold value $Ri_{cr} = 0.45$ (Lemarié et al. 2012), as described in Large et al. (1994), parameterizing the effect of three-dimensional vertical shear instabilities that cannot be resolved by the hydrostatic dynamics. The domain, which has open boundaries on all sides, is 320 km ($\approx 21L$) in the along-flow direction and 260 km ($\approx 17L$) in the cross-flow direction. The seamount is placed in the middle of the domain along the x axis, but is located at $y = 7L$ from the inflow boundary, giving it about $13L$ downstream development. Radiative open boundary conditions are used with adequate sponge layers as detailed in Mason et al. (2010). Tests were performed by doubling the flow domain size, while keeping the resolution fixed; this resulted in marginal differences in the wake structure, thereby ensuring that the upstream and side boundary conditions do not affect the flow in the domain. The horizontal resolution is fixed at $\Delta x = 350$ m for all solutions discussed in this study, resulting in a grid size of 915×740 points in the horizontal. Because the model is terrain following, the bottommost σ level ($\sigma = 0$) corresponds to the ocean bottom, $z(\sigma = 0, x, y) = h_b(x, y)$, while the topmost σ level matches the free surface. A total of 120 σ levels are used, resulting in a vertical grid spacing that varies from 1 m on the flat bottom to around 0.7 m at the top of the seamount itself. The grid is also highly stretched toward the bottom to ensure resolution of the BBL; the ROMS grid parameters are $\theta_s = 1$ and $\theta_b = 6$ [for a description of the ROMS vertical grid structure and the meaning of these parameters, see Shchepetkin and McWilliams (2009)].

d. Eddy integral scales

We use eddy integrals scales defined in S19 for examining the horizontal and vertical length scales in the wake as a function of downstream distance y location. The inverses of these integral scales are defined as

$$\frac{1}{L^I(y)} = \frac{1}{2\sqrt{2}T} \int_{t_0}^{T+t_0} \left[\frac{\int \zeta'^2 dx dz}{\int \text{EKE} dx dz} \right]^{1/2} dt, \quad (11)$$

$$\frac{1}{H^I(y)} = \frac{1}{2\sqrt{2}T} \int_{t_0}^{T+t_0} \left[\frac{\int U_z'^2 dx dz}{\int \text{EKE} dx dz} \right]^{1/2} dt. \quad (12)$$

Here, the eddy vorticity, $\zeta' = v'_x - u'_y$, eddy vertical shear, $U_z'^2 = u_z'^2 + v_z'^2$, and eddy kinetic energy, $\text{EKE} = u'^2 + v'^2$, are based on velocity fields computed relative to a time-mean, $(u', v') = (u, v) - (\bar{u}, \bar{v})$, where $(\bar{u}, \bar{v}) = (1/T) \int_0^T (u, v) dt$. The factor of $2\sqrt{2}$ is based on the expected result for an idealized, localized Gaussian eddy (i.e., for an idealized two-dimensional flow, $U(x, z) = U_0 \exp[-(x^2/l_x^2 + z^2/l_z^2)]$, we recover $L^I = 2l_x$ and $H^I = 2l_z$). The averaging interval T is one year (in non-dimensional units, $UT/L \approx 200$) with a startup time t_0 of 2 months.

e. Vertical enstrophy, ζ^2 , equation

The three-dimensional vorticity under the hydrostatic approximation takes the form $\boldsymbol{\omega} = (v_x - u_y)\mathbf{i} - u_z\mathbf{j} + v_z\mathbf{k}$, where $\zeta = v_x - u_y$ is the vertical vorticity. We find it instructive to examine the evolution of the vertical enstrophy ζ^2 and the horizontal enstrophy (equivalently the squared vertical shear, $\|\mathbf{v}_z\|^2 = u_z^2 + v_z^2$), because nonzero values of these shears are only generated on interaction with the seamount. Both these equations are directly derived from the hydrostatic primitive equations. The equation for ζ^2 takes the form

$$\frac{1}{2} \frac{D\zeta^2}{Dt} = \underbrace{\zeta(\zeta + f)w_z}_{\Omega_s} + \underbrace{\zeta(u_z w_y - v_z w_x)}_{\Omega_t} + \underbrace{\zeta \nabla \times \boldsymbol{\tau}_z \cdot \hat{\mathbf{k}}}_{\Omega_{\text{vmix}}} + \underbrace{\zeta D_h(\zeta)}_{\Omega_{\text{hdiff}}}, \quad (13)$$

where Ω_s and Ω_t are the vortex stretching and tilting terms, respectively. The dissipation terms are the horizontal hyper-diffusion term Ω_{hdiff} and the vertical mixing term from KPP Ω_{vmix} , with the interior viscous stress, $\boldsymbol{\tau} \equiv (\nu \partial_z u, \nu \partial_z v)$. The vertical mixing coefficient $\nu(z)$ comprises the effects of BBL parameterization on the slopes and interior parameterizations that control density overturns and vertical shear instabilities [like, for example, Kelvin–Helmholtz (KH) instabilities] through a gradient Richardson number criterion. As in the preceding section, we examine time averaged x, z integrals [$\langle \cdot \rangle = (1/T) \int_{t_0}^{T+t_0} \int_{-L_x/2}^{L_x/2} \int_{-h_b}^0 (\cdot) dx dz dt$] of these quantities to highlight their downstream (y) evolution. The averaging time is chosen to be 1 year in physical time or in nondimensional form, $UT/L \approx 200$. With the averaging performed, the Ω_{vmix} term can be further decomposed (see the appendix for details) as

$$\langle \Omega_{\text{vmix}} \rangle = \underbrace{\frac{1}{T} \int_{t_0}^{T+t_0} \int_{-L_x/2}^{L_x/2} \zeta_b \left(\frac{\partial \boldsymbol{\tau}}{\partial z} \Big|_b \times \nabla h_b - \nabla \times \boldsymbol{\tau}_b \right) \cdot \hat{\mathbf{k}} \, dx \, dt}_{\Omega_{\text{bot}}} - \underbrace{\langle \zeta_z \nabla \times \boldsymbol{\tau} \rangle \cdot \hat{\mathbf{k}}}_{\Omega_{\text{vmix,int}}}, \quad (14)$$

where Ω_{bot} denotes the bottom flux of enstrophy and $\Omega_{\text{vmix,int}}$ its interior dissipation due to vertical mixing. It is therefore appropriate to include the total interior dissipation term

$$\Omega_{\text{diss}} = \Omega_{\text{vmix,int}} + \Omega_{\text{hdiff}}. \quad (15)$$

Note that the bottom enstrophy generation term Ω_{bot} in (14) is comprised of two terms, one relating to the divergence of bottom stress ($\boldsymbol{\tau}_{z,b} \times \nabla h_b \cdot \hat{\mathbf{k}}$) and the second due to the bottom stress curl ($\nabla \times \boldsymbol{\tau}_b \cdot \hat{\mathbf{k}}$).

f. Horizontal enstrophy, $u_z^2 + v_z^2$, equation

Similarly an equation for the horizontal enstrophy (or squared vertical shear, $\|\mathbf{v}_z\|^2 = u_z^2 + v_z^2$) takes the form

$$\frac{1}{2} \frac{D \|\mathbf{v}_z\|^2}{Dt} = - \left[\underbrace{(u_z^2 u_x + v_z^2 v_y)}_{\Lambda_h} + u_z v_z (u_y + v_x) + \underbrace{\|\mathbf{v}_z\| w_z}_{\Lambda_v} \right] - \underbrace{(b_x u_z + b_y v_z)}_{-\Lambda_b} + \underbrace{D_v(\mathbf{u}_z)}_{\Lambda_{\text{vmix}}} + \underbrace{D_h(\mathbf{v}_z)}_{\Lambda_{\text{hdiff}}}. \quad (16)$$

Here $\Lambda_{nl} = \Lambda_h + \Lambda_v$ is the Lagrangian rate of change of vertical shear purely due to advective processes; Λ_h is the vertical shear generation due to the horizontal straining terms v_y, u_x , and $u_y + v_x$, while Λ_v represents the same but due to the vertical straining w_z . The term $D_v(\mathbf{v}_z)$ includes the changes induced by the vertical mixing and $D_h(\mathbf{v}_z)$ by the horizontal hyperdiffusion-like term that appears as part of the upwind-biased advective scheme. The vertical mixing term Λ_{vmix} can be expanded further in analogous fashion to (14) (detailed in the appendix) as

$$\langle \Lambda_{\text{vmix}} \rangle = \frac{1}{T} \int_{t_0}^{T+t_0} \int_{-L_x/2}^{L_x/2} \underbrace{\kappa u^* \|\mathbf{v}_z\|_{z=-h_x}^2}_{\Lambda_{\text{vmix,bot}}} dx \, dt + \underbrace{\langle \nu (u_z u_{zzz} + v_z v_{zzz}) \rangle}_{\Lambda_{\text{vmix,int}}}, \quad (17)$$

where $u^* = \sqrt{\tau_b}$ and κ are defined in (10). Further details on how the terms $\Lambda_{\text{vmix,bot}}$ and $\Lambda_{\text{vmix,int}}$ are evaluated numerically are provided in the appendix. In a similar fashion to (15), the interior shear dissipation is

$$\Lambda_{\text{diss}} = \Lambda_{\text{vmix,int}} + \Lambda_{\text{hdiff}}. \quad (18)$$

The vertical shear equation (16) is closely related to the frontogenetic tendency equation describing the evolution of the horizontal buoyancy gradients (Hoskins and Bretherton 1972). In fact, the two equations are identical in the inviscid,

quasigeostrophic limit, because the thermal wind relation means that, $\|\mathbf{v}_z^{\text{QG2}}\| = f^2 |\nabla b|^2$, and the buoyancy term in (16) vanishes. Equation (16) will be used to diagnose the generation of BBL vertical shear on the topographic slope and its subsequent downstream evolution in the wake. This approach parallels the one used by Dong et al. (2007) to characterize vorticity generation and evolution in submesoscale island wakes.

g. Energy conversion from mean-flow to the eddies

Decomposing the flow variables in the form, $\mathbf{u} = \mathbf{u}' + \bar{\mathbf{u}}$, where the bar denotes a long time-mean, we can write the evolution equation of the EKE in the form (Harrison and Robinson 1978)

$$\frac{\partial \frac{1}{2} (\overline{u^2} + \overline{v^2})}{\partial t} + \frac{\partial \frac{1}{2} \left(\overline{u_j u_j^2} + \frac{1}{2} \overline{u_j^2 u_j^2} + \frac{1}{\rho_0} \overline{u_j^2 p'} \right)}{\partial x_j} = \underbrace{-\overline{u'_i u'_j} \frac{\partial \overline{u_i}}{\partial x_j}}_{K_m K_e} + \overline{w' b'} - \varepsilon. \quad (19)$$

The transport term uses indicial notation, so that $(u_1, u_2, u_3) = (u, v, w)$. The mean-to-eddy kinetic energy transfer term can be decomposed as $K_m K_e = \text{HRS} + \text{VRS}$ to separate the effect of horizontal and vertical shear stress terms,

$$\text{HRS} \equiv -(\overline{u' u' u_x} + \overline{u' v' u_y} + \overline{v' v' v_y} + \overline{u' v' v_x}), \quad (20)$$

and

$$\text{VRS} = -(\overline{v' w' v_z} + \overline{u' w' u_z}). \quad (21)$$

The term $\overline{w' b'}$ represents the conversion term from the eddy available potential to the eddy kinetic energy term, where $b = -(g/\rho_0)\rho'$ is the buoyancy. The dissipation term ε measures the kinetic energy losses due to parameterized vertical mixing in the model and the implicit biharmonic model diffusion; a part of ε is also converted back to potential energy.

3. Phenomenology of the equatorial wake transition

In this section we characterize and quantify the changes in wake structure as a function of Ro_L . Mirroring the methodology of S19, we start by examining the BBL separation and instability on the slopes of the seamount and its subsequent downstream evolution. We find in particular a progressive increase in the wake vertical shear as Ro_L is increased, which manifests as highly layered quasi-horizontal vortical structures. Finally, we use integral scales defined in (11) and (12) to quantify the horizontal and vertical eddy sizes, and eddy aspect ratios as a function of Ro_L .

a. Departure from steady quasigeostrophic flow

S19 examined the wake structure for fixed $\text{Ro}_L = 0.1$ and $\hat{h} \in [0.1, 4.7]$ (obtained by fixing all other parameters and varying the stratification). For a small nondimensional height value of $\hat{h} \approx 0.1$, they found that the flow converged to the

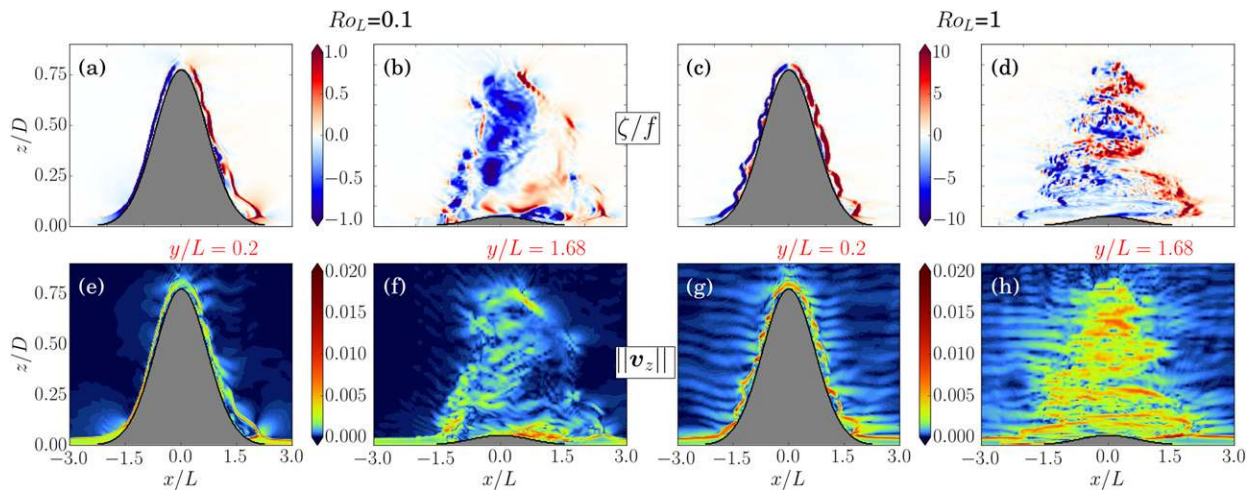


FIG. 2. Downstream evolution of vertical vorticity and vertical shear: x - z sections of (a)–(d) ζ/f and (e)–(h) $|\mathbf{v}_z| = \sqrt{u_z^2 + v_z^2}$ (s^{-1}) for a snapshot of the flow for different values of $\text{Ro}_L = 0.1$ and $\text{Ro}_L = 1.0$. Two downstream locations, $y/L = 0.2$ and $y/L = 1.68$, are chosen to highlight BBL separation and the formed wake immediately downstream of the seamount slope. Note that the ζ/f color bars have larger ranges to reflect the change in f while the $|\mathbf{v}_z|$ color bars are identical. The background flow is into the page.

classical steady quasigeostrophic (QG) solution of an anticyclone over the seamount (Schär and Davies 1988). As \hat{h} was increased, BBLs on the slopes were found to separate, become unstable, and roll up, leading to the formation of wake SCVs. In particular they found that robust eddying regimes required $\hat{h} > 1$. Here keeping $\text{Fr}_v = 0.02$ ($s = 4.7$) fixed, and systematically decreasing Ro_L (by increasing f), the steady QG anticyclone is observed at around $\text{Ro}_L \sim 0.005$, again corresponding to $\hat{h} \approx 0.1$ (not shown). This is expected from the results of Schär and Davies (1988), who found that the existence of steady QG solutions required $\hat{h} = \text{Ro}_L s < O(1)$ and $\text{Ro}_L \ll 1$. Thus, the limiting QG solution should be recoverable by either fixing $\text{Ro}_L \ll 1$ and decreasing s (as is done in S19) or by fixing s and decreasing Ro_L , as is done here. Interestingly, starting from the numerically observed steady QG solution at $(\hat{h}, s, \text{Ro}_L) = (0.1, 1, 0.1)$ and systematically increasing Ro_L smoothly leads to the steady lee wave regime (not shown). Our current study is similar but instead at the much larger value of $s = 4.7$ ($\text{Fr}_v = 0.002$). Because the departure from QG has been already detailed in S19, we do not belabor that point here. Instead we start at $\text{Ro}_L = 0.1$ when the wake manifests highly coherent, vertically aligned SCVs (see S19 for details) and increase Ro_L (decrease f) instead to examine the equatorial transition in the wake.

b. BBL separation and the near-wake structure, $y/L < 2$

Figure 2 highlights the evolution of the wake immediately after BBL separation on the slopes ($y/L = 0.2$) and further downstream ($y/L = 1.68$) for the two values of $\text{Ro}_L = 0.1$ and $\text{Ro}_L = 1$. The separated shear layer vorticity (Figs. 2a,c) has a similar range of values in the two cases, although $\text{Ro}_\zeta \sim 1$ when $\text{Ro}_L = 0.1$ and $\text{Ro}_\zeta \sim 10$ when $\text{Ro}_L = 1$, a direct consequence of the tenfold variation in f . The $\text{Ro}_L = 0.1$ case shows vertical and horizontal coherence starting to develop at $y/L = 1.68$ (Figs. 2b) due to the wake upscaling and alignment mechanisms

demonstrated in S19. However, the $\text{Ro}_L = 1.0$ near-wake (Fig. 2d) lacks such a coherence, instead consisting of great deal of finescale structure in both the horizontal and vertical directions. The near-wake vertical shear changes are even more dramatic. While the separated BBL vertical shear in the two cases (Figs. 2e,g) have a similar range of values (with differences caused by an evidently faster BBL instability for larger Ro_L), the near-wake shear values (Figs. 2f,h) are substantially larger for the larger Ro_L case. In particular, the $\text{Ro}_L = 1$ case displays a highly layered structure with strong vertical shear. Furthermore, the vertical shear values are equally strong in both cyclonic and anticyclonic regions.

A three-dimensional view of the wake comparing $\text{Ro}_L = 0.1$ and $\text{Ro}_L = 1$ is presented in Fig. 3 and confirms the tilted layering of the wake and its finescale structure downstream of the seamount. However, what is also evident here is the near wake instability. S19 first highlighted the spiral bands in the wake that seem to characterize the instability mode of separated bottom boundary layers off the slope. These bands spiral downward while at the same time undergoing filamentation. Figure 3 illustrates the role of changing f on the spiral bands in the sense that they become progressively more horizontal. In other words, the ratio of the horizontal to vertical scales of the instability increases with Ro_L (see next section for a quantification of this observation). The precise nature of this instability mode and its dependence on f and N currently remains obscure and requires further investigation.

c. Far-wake structure

Figure 4 offers a more detailed view of the shear and vorticity downstream of the seamount. Figures 4a,d,g,j recapitulate the results in S19, showing coherent $\text{Ro}_\zeta \sim 1$ SCVs with a persistent vertical alignment that are fully formed within a short distance downstream of BBL separation. As seen previously in Fig. 2, with increasing Ro_L finescale structure is

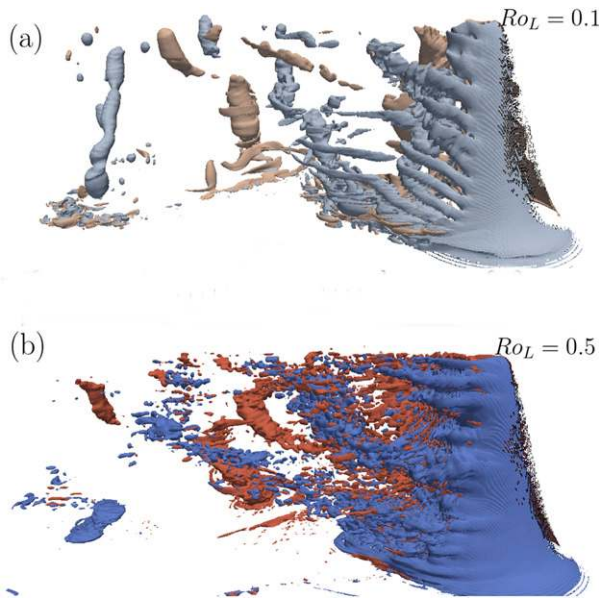


FIG. 3. Three-dimensional vortical wake structure for (a) $Ro_L = 0.1$ and (b) $Ro_L = 0.5$. The isosurfaces in (a) have values $\zeta/f = \pm 0.5$, and in (b) $\zeta/f = \pm 2$. In both panels, blue colors represent negative values and red colors, positive values. The barotropic inflow is from right to left.

observed in the horizontal sections (Figs. 4a–c) both in the near-wake and also well downstream of the seamount, especially when $Ro_L = 1.0$. This finescale structure is observed in both the cyclones and anticyclones (a significant point that is explained later). Also of note in the topmost row of Fig. 4 is the observation that the horizontal sizes of the wake SCVs, especially evident in the far-wake, are largest for $Ro_L = 1.0$. The corresponding horizontal sections of the vertical shear are shown in Figs. 4d–f and display a monotonic increase from left to right, reflecting the results in Fig. 1 and concomitant with the increasing finescale structure in the vorticity.

The y – z sections of the vorticity and vertical shear show a systematic tilting and layering with increasing Ro_L (Figs. 4g–i). These layers are almost quasi-horizontal when $Ro_L = 1.0$, a fact that is somewhat obscured by the plotting in nondimensional coordinates in Fig. 4. More precisely, the seamount aspect ratio h/L is around $\sim 3^\circ$ while the average slope of tilted shear layers in Figs. 4f and 4i is only around 0.1° . Thus decreasing f by a factor of 10 transforms the wake from being nearly vertically aligned to nearly horizontally aligned. In stratified vortical flows, the former are referred to as “columnar” vortices and the latter as “pancake” vortices (Beckers et al. 2001). Furthermore, the vertical shear in the wake interior (Figs. 4j–l) also progressively increases with Ro_L (note the increasing color bar ranges from left to right), which is also consistent with the formation of layers with fine horizontal structure. One consequence of this layering at larger values of Ro_L is that SCVs formed in each of these layers can be largely decoupled. Equivalently the phase of eddy shedding at different depths is not correlated. This observation was recorded in a recent idealized study similar to the present one (Perfect

et al. 2018), where the authors characterize the dephasing of eddy generation through a vertical Strouhal number that nondimensionalizes the shedding frequency at each depth. The layering phenomenon and the decoupling of vortical dynamics between layers was first documented by Lilly (1983), who suggested that it was a consequence of evolution of turbulence in a stratified background. It has been well documented in idealized homogeneous rotating-stratified turbulent flows in both paradigms of forced-dissipative (Waite and Bartello 2006; Marino et al. 2013) and decaying turbulence (Praud et al. 2006). These studies also find a monotonic decrease in layer thickness as a function of f , with the layer thickness being smaller than the forcing thickness for small enough f (Marino et al. 2013). These layers superficially resemble internal-wave fronts; however, this is illusory because the shear layers simply advect downstream with the flow instead of propagating like waves. Also, because the vertical Froude number is small ($Fr_v = 0.02$), direct generation of internal lee waves at the topography is negligible and not energetically important, as described by Perfect et al. (2020b), even though the waves can be noted visually in Fig. 4f.

The far-wake vertical shear and vorticity magnitudes are quantified in Fig. 5 through their respective root-mean-square (rms) values, $\zeta^{rms} = \sqrt{\int \zeta^2 dV}$ and $v_z^{rms} = \sqrt{\int (u_z^2 + v_z^2) dV}$ where the volume of integration excludes the regions $y/L < 4$ and $z < 50$ m (the abyssal BBL). Clearly v_z^{rms} monotonically increases with Ro_L , consistent with Figs. 4g–i, while ζ^{rms} does the same but only weakly so. In agreement with S19, the abyssal BBL approximately scales as $h_{bbl} \approx 3u^*/\sqrt{Nf}$. Thus, the BBL vertical shear has the scaling $U_{z,bbl} \sim U/h_{bbl} \sim \sqrt{Nf}$ and so does the BBL vorticity multiplied by $\theta_b \sim \alpha$, the aspect ratio [given the topographic constraint (2)]. If the BBL vertical shear was also the source for the interior vertical shear, then we would expect v_z^{rms} to monotonically decay as \sqrt{f} as $f \rightarrow 0$; however, it has the opposite behavior. This finding lends itself to the hypothesis that the vertical shear (and the layer formation) is in fact generated in the flow interior downstream of separation. We explicitly demonstrate that this is in fact the case in subsequent sections.

d. Horizontal and vertical eddy scales

To better quantify the visual perspectives gleaned in the previous section, we employ the eddy integral scales defined in (11) and (12). Figure 6 shows the downstream dependence of the horizontal and vertical integral scales, L^I and H^I . In both cases the trends are rather clear: L^I increases monotonically with y for all values of Ro_L . This follows from the mechanism of vortical filaments, formed by shear layer instability, that merge to form coherent SCVs. What Fig. 6 illustrates in particular, is that the merger process continues further downstream as Ro_L increases; i.e., for $Ro_L = 0.05$, the L^I curve has approximately reached its maximum value around $y/L = 5$, but when $Ro_L = 1.0$, the corresponding curve only asymptotes around $y/L = 10$. This is likely because the higher degree of filamentation in the higher Ro_L cases takes a longer time (translating to longer downstream distance) for the merger process to complete. The corresponding vertical scale H^I has the opposite trend; the smallest scales are found for the largest

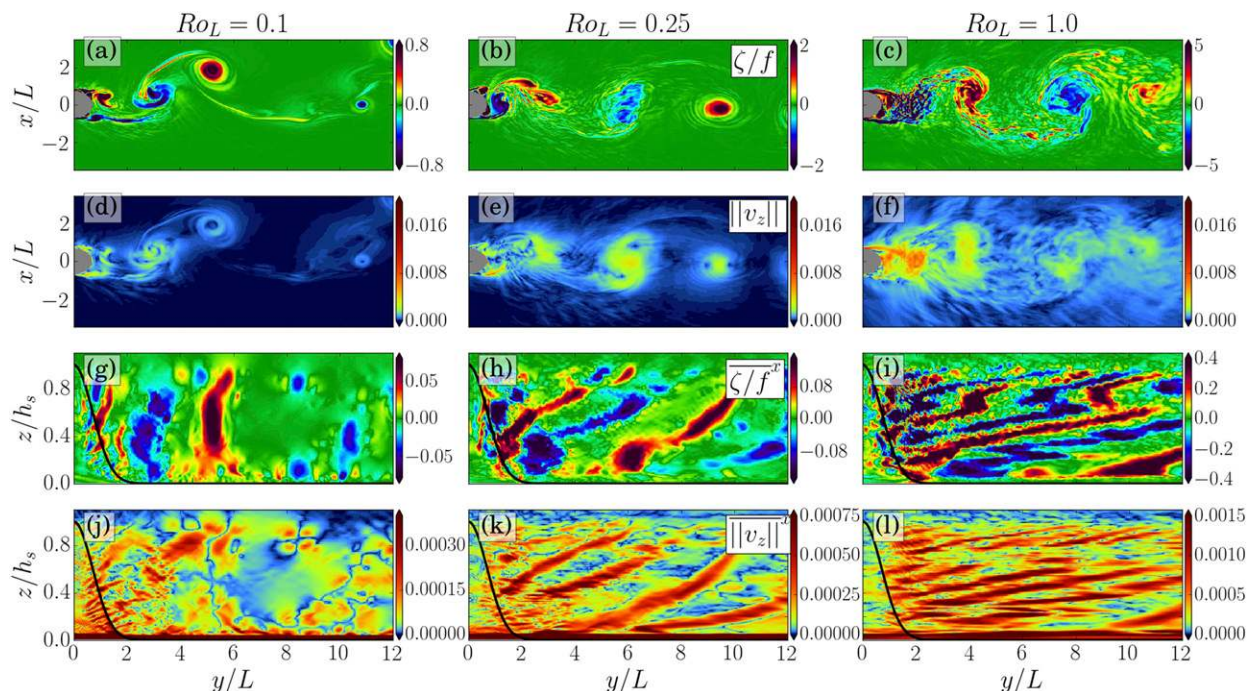


FIG. 4. Vorticity and vertical shear snapshots in wake, for three different values of (from left to right) $Ro_L = 0.1, 0.25, 1.0$. Horizontal sections of (a)–(c) ζ/f and (d)–(f) $\|v_z\|$ (s^{-1}) at $z = 500$ m from bottom. Cross-stream, i.e., x -averaged (g)–(i) vorticity $\bar{\zeta}^x/f$ (s^{-1}) and (j)–(l) vertical shear $\|\bar{v}_z\|^x$ (s^{-1}). The barotropic background flow is from left to right of each plot. Note that the color bar ranges increase from left to right (i.e., with increasing Ro_L) except in (d)–(f).

Ro_L case. This is expected with the progressively increased layering of the wake found in Fig. 4: H^I thus captures the vertical scales of the layers. The vertical scale in the far wake varies between about a third of the seamount height at $Ro_L = 0.05$ ($\hat{h} = 2.35$) to around a tenth of h_s when $Ro_L = 1$ ($\hat{h} = 47$).

S19 found similar results, increasing far-wake L^I and decreasing far-wake H^I with \hat{h} . Here we find a continuation of these trends when we note that increasing Ro_L and fixing s also causes \hat{h} to increase. This allows us to posit the question as to whether, in this region of parameter space, the two parameter

family (Ro_L, s), can actually be reasonably represented only by \hat{h} . We return to this question repeatedly in subsequent sections.

The trends in L^I and H^I can favorably be compared with studies of decaying turbulence in rotating-stratified flows (Praud et al. 2006; Marino et al. 2013). Praud et al. (2006) in particular find in their experimental study of decaying grid turbulence that horizontal integral scales increase with N/f and vertical integral scales decrease with N/f . This is consistent with both the present study and S19, where \hat{h} is essentially a proxy for N/f , because we hold the seamount aspect ratio α constant.

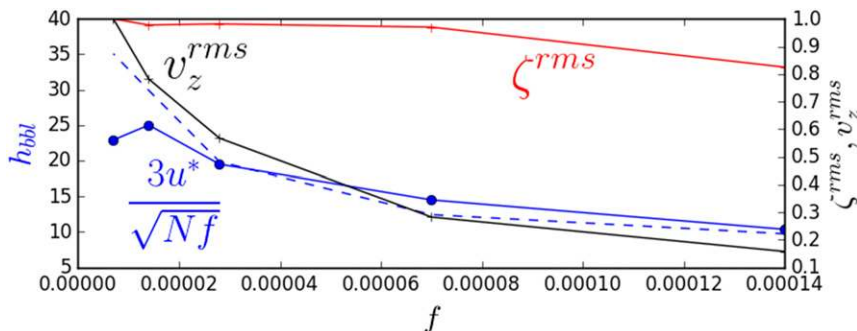


FIG. 5. BBL depth h_{bbl} (m) (blue solid curve) as a function of f (s^{-1}) on the flat bottom, away from the seamount. Also shown is the volume averaged, root-mean-square vorticity and vertical shear, $(\zeta_{rms}, v_{z,rms}) = \sqrt{(1/V) \int (\zeta^2, u_z^2 + v_z^2) dV}$ normalized by their respective values at the smallest f value. Here V represents the far-wake region of the seamount but excluding the abyssal BBL $y/L > 4, z > 50$ m. The dashed blue curve shows $3u^*/\sqrt{Nf}$.

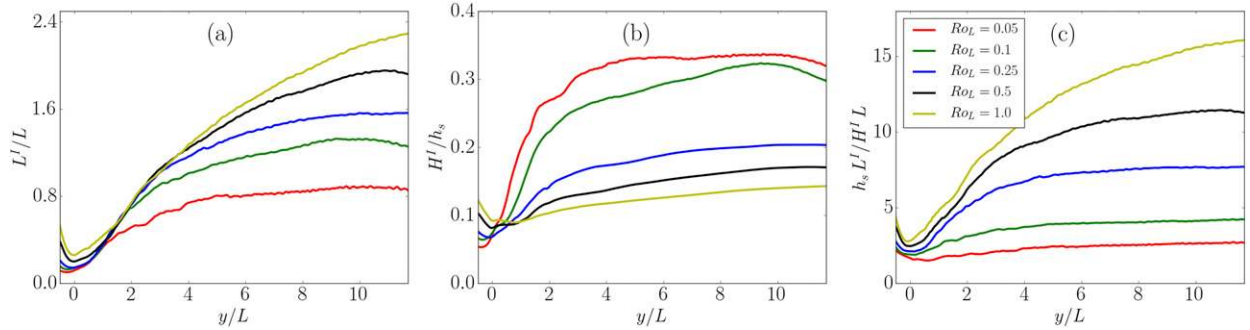


FIG. 6. The integral length scales defined in (11) and (12) as a function of downstream distance y/L : (a) L^I/L , (b) H^I/h_s , and (c) the average wake aspect ratio $h_s L^I/H^I L$.

The variation of far-wake H^I with Ro_L is shown in Fig. 7: for $Ro_L < 0.5$, it approximately satisfies

$$H^I \sim \frac{1}{6} \sqrt{\frac{f}{N}}, \quad (22)$$

which is the empirical scaling discovered in S19 for $Ro_L = 0.1$ and $\hat{h} \in [1, 4.7]$. Figure 7 shows that this scaling is in fact valid in the larger parameter range of Ro_L and $\hat{h} \in [2, 47]$. As a contrast, the geostrophic scaling $H^I \sim fL^I/N$ is also shown. This underscores the result that in spite of significant differences in the wake structure from $Ro_L = 0.1$ to $Ro_L = 0.5$ (as seen in Fig. 4), the dynamics governing the equilibrated SCVs might be the same one. Furthermore, H^I seems to asymptote to an f -independent value beyond $Ro_L = 1.0$. In rotating stratified turbulence studies (Waite and Bartello 2006; Praud et al. 2006), the integral scales were found to vary from fL^I/N when the rotation is strong to V_e/N once the rotation is sufficiently weakened, where V_e is a velocity scale corresponding to turbulent eddies. The latter scale implies that the vertical Froude number of turbulence, $V_e/NH^I \sim 1$, a well observed characteristic of nonrotating stratified turbulent flows. Using the value of $H^I \approx 120$ m from the $Ro_L = 1.0$ case, we get a velocity scale $V_e \approx 0.7 \text{ m s}^{-1}$, which is larger than the observed eddy velocities of $\approx 0.2 \text{ m s}^{-1}$. Thus, computations at smaller values of f might be needed to establish the actual asymptotic value of H^I . Alternatively this might reflect the limitations of using the primitive equations instead of Boussinesq equations (at significantly higher horizontal resolutions) in simulating weakly rotating, stratified flows (see the extended discussion on this topic in section 5c).

4. Energy and enstrophy: Sources and sinks

In this section we attempt to explain the observations in the previous section directly by examining the balances of the enstrophy (horizontal and vertical) and the eddy kinetic energy. All these three quantities are absent in the barotropic inflow and are only generated on interaction with the seamount. Further the expected instabilities in the wake are those due to negative potential vorticity in anticyclones [characterized by S19, Molemaker et al. (2015), and Gula et al. (2016)] and vertical shear instabilities typical of stratified turbulent and

wake flows, both of which are parameterized in hydrostatic ROMS. We characterize the sources and sinks of enstrophy at the seamount slope and the interior and show that they can explain the observed EKE dissipation in the wake due to the aforementioned instability mechanisms.

a. Bottom generation of vertical enstrophy

The dominant terms that constitute the vertical enstrophy equation (13) are plotted as a function of downstream distance y/L in Fig. 8 for values of Ro_L between 0.05 and 1.0. The largest term is the bottom generation term (Ω_{bot} , (14), which is predominantly positive in the region $-2 < y < 0$, i.e., on the seamount slopes upstream of the centerline. This is because the flow starts undergoing separation from the bottom slope around $y > 0$ (as visualized in Fig. 2), shutting down vorticity generation. An exception is a smaller generation bump peaking around $y/L = 1$ due to secondary BBLs induced by the wake eddies as they separate from the seamount. These secondary BBLs on the downstream slopes ($y > 0$) have opposite signed vorticity to the dominant local generation (i.e., cyclonic on the anticyclonic side $x < 0$ and vice versa) but are weaker

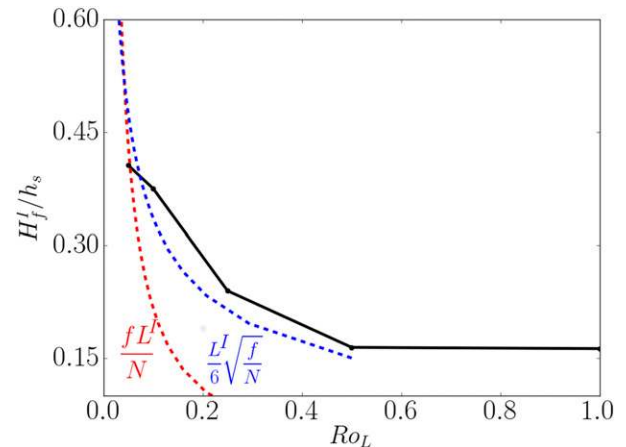


FIG. 7. The variation of far-wake vertical integral scale H^I/h_s as a function of the seamount Rossby number, Ro_L . Also shown are the predictions from QG scaling fL^I/N and the empirical scaling from S19, $L^I/6\sqrt{f/N}$.

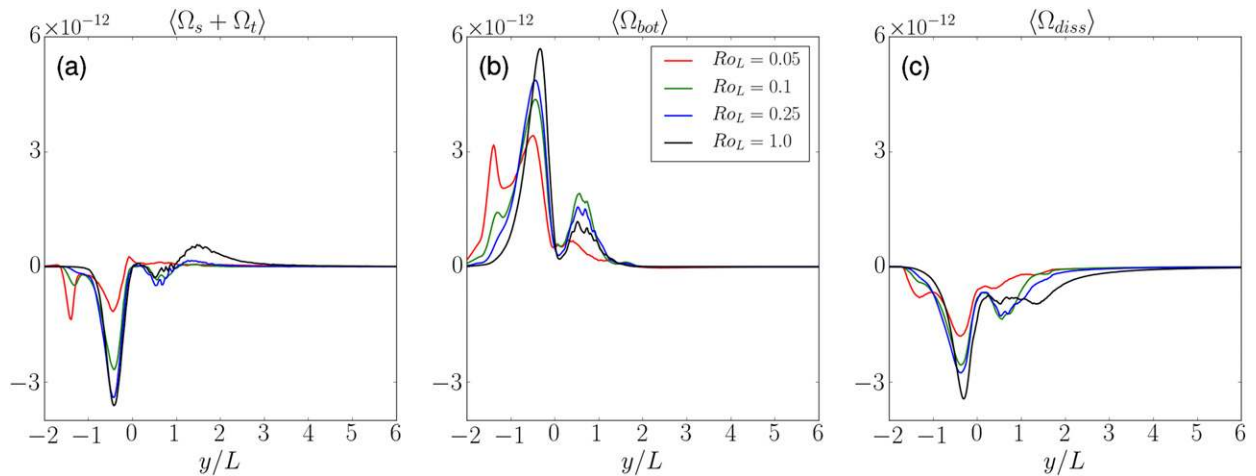


FIG. 8. Vertical entrophy balance: The dominant terms of the time and (x, z) -averaged vertical entrophy equation (13): (a) the vortex stretching and tilting terms $\langle \Omega_s + \Omega_t \rangle$ (s^{-2}), (b) the bottom generation term $\langle \Omega_{bot} \rangle$ (s^{-2}) (14), and (c) the interior entrophy dissipation term $\langle \Omega_{diss} \rangle$ (s^{-2}) (15).

than the primary BBLs on the upstream slopes ($y < 0$). Last, we note that of the two terms that comprise $\langle \Omega_{bot} \rangle$, (14), the generation due to bottom stress divergence ($\tau_{z,b} \times \nabla h_b \cdot \mathbf{k}$) is an order of magnitude larger than that due to the bottom stress curl ($\nabla \times \tau_b \cdot \mathbf{k}$). This is a significant point but ancillary to the discussion here and its relevance is addressed in a concurrent study (Jagannathan et al. 2021).

There are two sinks of entrophy, the first of which is the sum of the vortex stretching and tilting terms $\langle \Omega_s + \Omega_t \rangle$. While not shown due to lack of relevance, $\langle \Omega_s \rangle > 0$ is a source and $\langle \Omega_t \rangle < 0$ a sink of entrophy. The interior dissipation term $\langle \Omega_{diss} \rangle$, (15), has a similar order of magnitude as the advective sink, and like the generation term has a secondary bump around $y/L = 1$. It should be noted that both the advective sink $\langle \Omega_s + \Omega_t \rangle$ and the dissipation $\langle \Omega_{diss} \rangle$ are predominantly localized to the generation, i.e., happens at almost the same downstream location. It is notable that the variation of each of these quantities is only marginal with increasing Ro_L , which is particularly evident for $Ro_L > 0.1$; in fact, peak values of generation from $Ro_L = 0.1$ to $Ro_L = 1$ show only a 20% increase. This finding is consistent with results in Fig. 5, demonstrating a similar 20% change in ζ^{rms} with Ro_L over the same range. It is interesting that a significant fraction of the bottom-generated entrophy is dissipated locally and the remainder is what is contained in the wake SCVs that are advected downstream (i.e., the residual of the terms shown in Fig. 8).

b. Interior generation of vertical shear

The vertical shear (or horizontal entrophy) has a significantly different balance compared to the vertical entrophy (as shown in Fig. 9). First, the bottom generation, $\langle \Lambda_{bot} \rangle$ (Fig. 9c) is negligible compared to the other terms in (16). This is in stark contrast to the entrophy that is generated at the bottom in BBLs and then advected into the flow through separation. In other words, BBL vertical shear is not the primary source of vertical shear observed downstream of separation.

The dominant term is in fact the horizontal advective term $\langle \Lambda_h \rangle$, which represents the change in the vertical shear due to the effect of the horizontal straining terms u_x, v_y , and $u_y + v_x$. This term drives interior generation of vertical shear downstream of the seamount centerline $x = 0$, resulting in the layered structure seen in Fig. 4. The shear change due to the vertical straining term $\langle \Lambda_v \rangle$ is in comparison negligible, as is the buoyancy term $\langle \Lambda_b \rangle$, and is consequently not shown. The interior advective generation term $\langle \Lambda_h + \Lambda_v \rangle$ as a function of downstream distance is shown in Fig. 9b displaying a strong dependence on Ro_L . Not only do the peak values in Fig. 9b increase by factor of 6 between $Ro_L = 0.1$ and $Ro_L = 1$, but a pronounced downstream shift in the respective peaks is observed, around $y/L = 0.2$ when $Ro_L = 0.1$ to around $y/L = 1.1$ when $Ro_L = 1$. This dependence on Ro_L clearly differs from that displayed by the vertical entrophy generation and dissipation, as detailed in the previous section, but is consistent with the Ro_L dependence of v_z^{rms} found in Fig. 5.

The increase in interior wake vertical shear with increasing Ro_L (i.e., weakening rotation) can be attributed to vortical wake instabilities similar to those observed in columnar vortices in stratified flows (Billant and Chomaz 2000; Deloncle et al. 2008; Waite and Smolarkiewicz 2008). In idealized settings columnar vortices and vortical pairs (with initially negligible vertical shear) have been shown to undergo instabilities that result in the formation of small vertical scales (with high vertical shear). Because the wake structure observed here shifts from columnar vortices with low vertical shear (when Ro_L is small) to layered pancake vortices with high vertical shear (when Ro_L is large), we suspect that similar mechanisms as those isolated in simple vortical stratified flows might be at play. In effect we hypothesize that the near wake increase of Λ_h (with a peak value that monotonically increases with increasing Ro_L) captures the effect of these instabilities.

The interior generation of high vertical shear results in small values of the gradient Richardson number $Ri_g = N^2/|\mathbf{v}_z|^2$ (discussed in detail in subsequent sections) triggering the

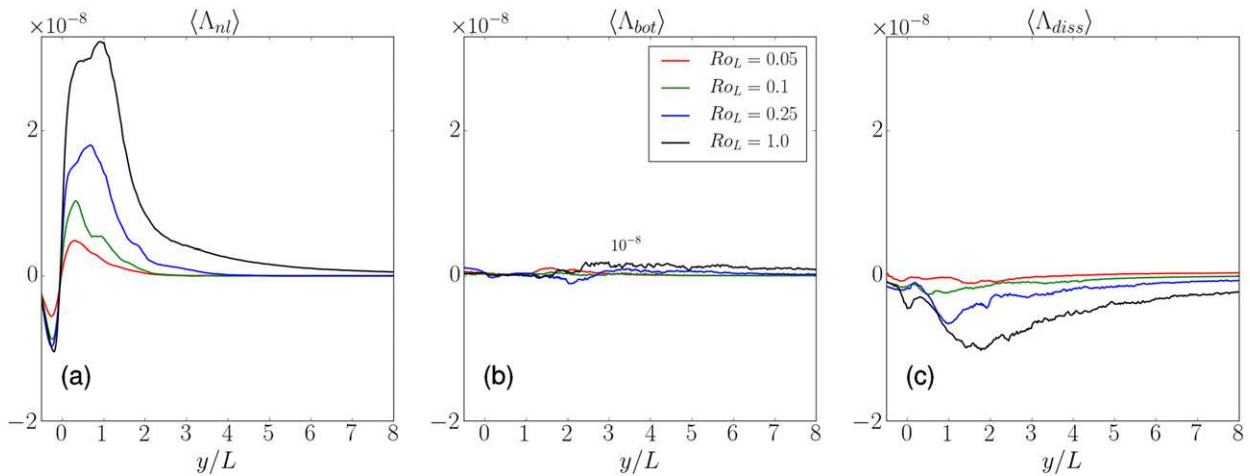


FIG. 9. Vertical shear balance: the dominant terms of the time and (x, z) -averaged vertical shear equation (16). (a) The nonlinear advective term comprising the horizontal and vertical straining effects $\Lambda_{nl} = \Lambda_h + \Lambda_v$ (s^{-2}). (b) The bottom generation term $\langle \Lambda_{bot} \rangle$ (s^{-2}) (17) and (c) the interior dissipation term $\langle \Lambda_{diss} \rangle$ (s^{-2}) (18). The buoyancy generation term $\langle \Lambda_b \rangle$ is negligible in comparison and has been omitted.

interior mixing parameterizations of the numerical model to be switched on, resulting in shear dissipation. As expected, the vertical shear dissipation Λ_{diss} , unlike enstrophy dissipation, is nonlocal and happens over a long downstream distance after the peak generation, as can be most clearly seen for the $Ro_L = 1$ case in Fig. 9c. Another physical interpretation of the interior generation of vertical shear by $\langle \Lambda_h \rangle$ as a forward cascade process and its consequences are discussed in the next section.

c. Eddy kinetic energy generation and dissipation

Previous studies (Dong et al. 2007; Gula et al. 2015a, 2016; Srinivasan et al. 2017) have consistently found that topographic wake eddies are generated by a horizontal shear instability mechanism inferred by the dominance of the $\langle HRS \rangle$ term in

the EKE balance equation (19). We find a similar balance here, as shown in Fig. 10. The dominant term for all values of Ro_L is the $\langle HRS \rangle$ term, the $\langle VRS \rangle$ being an order of magnitude smaller and hence not shown. $\langle HRS \rangle$ displays some minor variation with Ro_L , although the trends are difficult to discern. The baroclinic conversion term (Fig. 10b) is a factor of three or more smaller but is consistently negative, implying an energy conversion from kinetic energy to available potential energy (as a comparison, note that baroclinic instability shows a transfer in the opposite direction). This conversion is larger at smaller values of Ro_L but again does not exhibit a clear trend and is in fact largest at $Ro_L = 0.25$. The dominance of HRS even in the limit of large Ro_L might seem at odds with the dramatic increase in interior vertical shear in the wake (Fig. 4)

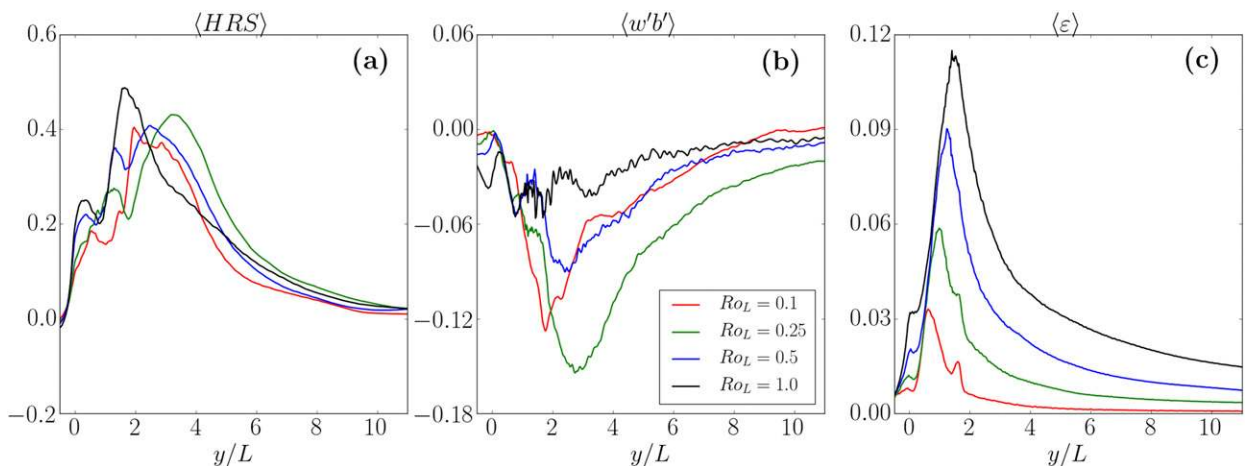


FIG. 10. EKE balance equation. The three most dominant terms of the time and (x, z) -integrated EKE equation (19): (a) the horizontal Reynolds stress term $\langle HRS \rangle$ (s^{-2}), (b) the baroclinic conversion term $\langle w'b' \rangle$ (s^{-2}), and (c) the energy dissipation (s^{-2}) due to the combined effects of parameterized vertical mixing and implicit horizontal hyperdiffusion. The term corresponding to the vertical Reynolds stress term, $\langle VRS \rangle$, is an order of magnitude smaller and consequently not shown here. Note the correspondence between the structure of the dissipative term here and the total vertical shear generation term in Fig. 9.

with increasing Ro_L . However, it is consistent with the fact that the dominant term in the vertical shear generation is $\langle \Lambda_h \rangle$, i.e., capturing the effect of horizontal straining terms on shear generation; it is just that the HRS is insufficient to discern the shift in the nature of the near-wake vortical instability mechanism as Ro_L increases.

The energy dissipation (Fig. 10c), however, shows a remarkable and consistent pattern of increase in peak magnitude and downstream shift of the peak with increasing Ro_L ; i.e., the wake dissipation has a larger magnitude and greater downstream extent for larger Ro_L . The clear trend in energy dissipation is at odds with the weak and nonmonotonic Ro_L variability in the $\langle HRS \rangle$ and $\langle w'b' \rangle$ terms and is likely not related to them dynamically. In fact the structure of the wake dissipation is comparable to the Ro_L dependence of the vertical shear generation (Fig. 9b). The fact that the peak value of the dissipation for each Ro_L in (Fig. 10c) is immediately downstream of the peak value of interior vertical shear generation suggests a causal relation between the two quantities. Conversely, the weak dependence of the enstrophy generation and dissipation on Ro_L (Fig. 8) implies that enstrophy dissipation might not be dynamically related to energy dissipation.

These results are also consistent with studies that examine the role of weakening rotation in idealized rotating-stratified turbulence. In these studies, weakening rotation induces a forward cascade of energy to small scales and subsequent dissipation through an enhancement of vertical shear leading to shear instabilities. Thus, the vertical shear generation terms $\Lambda_{nl} = \Lambda_h + \Lambda_v$ likely capture the effect of forward energy cascade processes that enhance vertical shear, subsequently leading to dissipation. An extended discussion on this topic is continued in section 5.

Following S19, we plot the volume integrated dissipation, $\langle \epsilon \rangle_V$ as a function of Ro_L in Fig. 11. The energy dissipation is found to increase by an order of magnitude for a similar increase in Ro_L . In S19, $\langle \epsilon \rangle_V$ was found to increase monotonically with increasing stratification N and, therefore, \hat{h} . Here the increase in $\langle \epsilon \rangle_V$ is found by decreasing f , which increases Ro_L and correspondingly, \hat{h} . This further supports the conjecture in section 2c that for $\hat{h} > 1$, wake dynamics might depend entirely on a single parameter \hat{h} instead of (Ro_L, Fr_v) . A similar hypothesis on \hat{h} dependence is suggested by Perfect et al. (2018) though they conjecture that this might be explained through Rossby wave dynamics which, given the results here is, unlikely.

Because (temperature and salinity) mixing typical accompanies dissipation, this result has potentially important implications for topography-induced mixing and water-mass transformation in tropical regions like the Solomon Sea that lie along key pathways for oceanic water masses (M  let et al. 2011; Germineaud et al. 2016).

5. Discussion

a. A submesoscale to stratified turbulence transition

The role of rotation in rotating-stratified turbulence has previously been examined in the context of forced-dissipative (Waite and Bartello 2006) and decaying turbulence paradigms

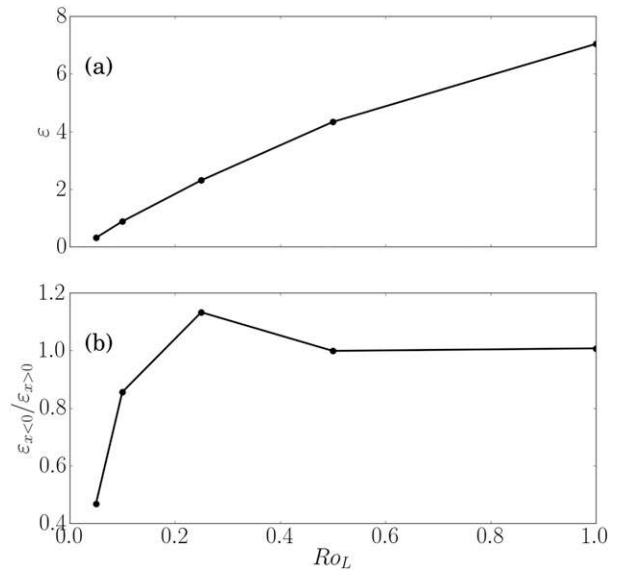


FIG. 11. (a) The volume integrated energy dissipation rate $\langle \epsilon \rangle_V$ (10^6 W) as a function of Ro_L . (b) The ratio of $\langle \epsilon \rangle_V$ contributions from the region $x < 0$ (approximately the anticyclonic side) and $x > 0$ (the cyclonic side) as a function of Ro_L , highlighting an initial anticyclonic-dominant dissipation which symmetrizes with increasing Ro_L .

(Praud et al. 2006; Marino et al. 2013). Here we make a connection between our results and these previous studies. First, we posit that topographic wake flows, as the one here, must be viewed as decaying turbulence flows (rather than forced-dissipative turbulent flow). This can be understood by transferring to the reference frame of the flow, wherein the topography injects wake vorticity at a given location and moves downstream, allowing free decay of the wake turbulence.

As noted in section 3d, the vertical integral scale H^I in classical freely decaying turbulent flows varies from fL^I/N when rotation is strong to V_e/N in the weakly rotating limit, where V_e is an integral eddy velocity scale. However, the dominant scaling law for $0.05 < Ro_L < 0.5$ found here is $H^I \sim L^I \sqrt{f/N}$, which was originally discovered by S19 for $Ro_L = 0.1$ and a range of Fr_v values. This raises the question of whether a geostrophic flow regime exists at all in vortical wakes that are generated by bottom drag separation and instability. Because BBLs have high horizontal and vertical shears purely due to their small vertical extent, vortices generated through this mechanism have $O(1)$ Ro_ζ values implying that such vortices are gradient-wind balanced rather than geostrophically balanced. In other words, eddy wake flows even in the $Ro_L \rightarrow 0$ limit have $Ro_\zeta \sim 1$, meaning that the fundamental characterization of wake flows as f varies is one of a transition from submesoscale turbulent wakes when $Ro_L \rightarrow 0$ to stratified turbulence as $Ro_L \rightarrow \infty$.

b. Route to dissipation: Parameterized centrifugal versus shear instability

Recent studies of flow–topography interactions (Gula et al. 2016; S19) find enhanced near-wake dissipation due to the

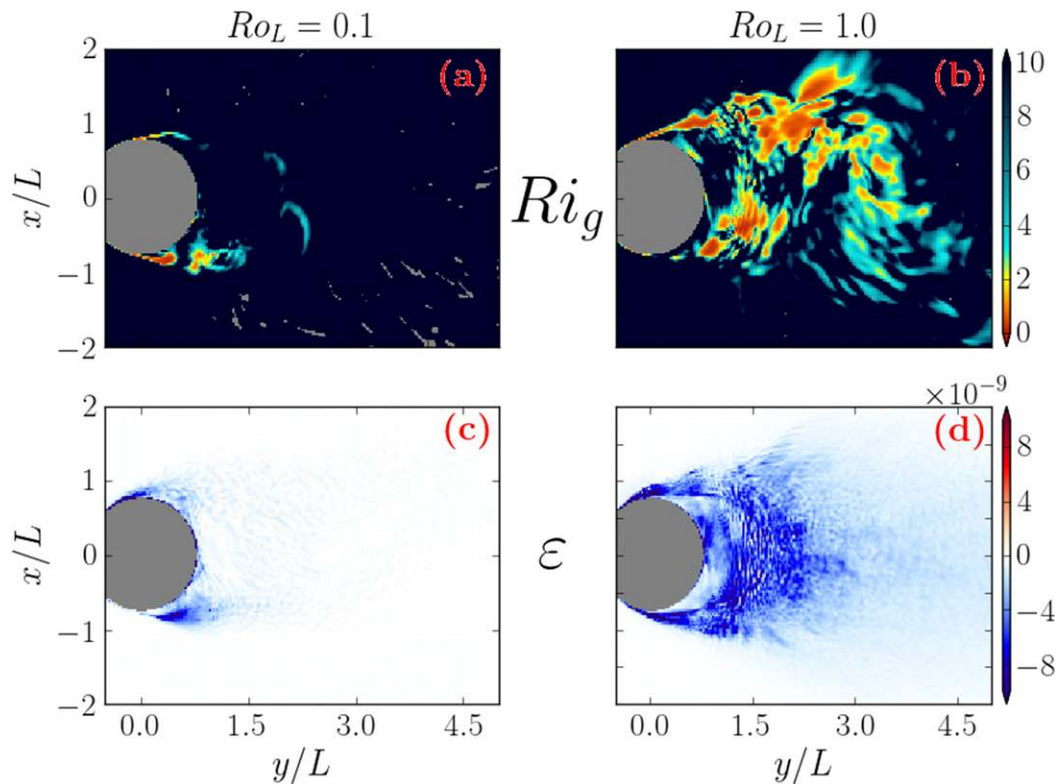


FIG. 12. Horizontal sections of (a),(b) snapshots of gradient Richardson number $Ri_g = N^2/|\mathbf{v}_z|^2$ and (c),(d) the energy dissipation rate ϵ ($m^2 s^{-3}$) at a depth of $z = -500$ m for two values of $Ro_L = 0.1$ and $Ro_L = 1.0$. Note the symmetrization of the dissipation pattern relative to the $x = 0$ axis, with increasing Ro_L .

presence of negative potential vorticity (pv) in anticyclones. This negative pv triggers centrifugal instabilities that generate small scales that are dissipated by the parameterized model mixing and diffusion. A direct connection between negative pv in the anticyclones and wake dissipation is made by (Molemaker et al. 2015; Gula et al. 2016; S19).

With increasing Ro_L (decreasing f), strong vertical shear is induced in the wake through advective cascade processes (section 4b), which in reality would induce three-dimensional vertical shear instabilities as is observed in stratified turbulence (Lilly 1983); three-dimensional vertical shear instabilities cannot be resolved by the hydrostatic model and are represented by parameterized mixing. In section 4c it is argued that the monotonic increase in wake dissipation (Fig. 11) is a direct consequence of the enhanced vertical shear and not the vorticity generation or dissipation (which directly relates to the pv).

Here we offer further support for this idea by examining the volume-integrated dissipation in broadly anticyclonic regions ($x < 0$) and broadly cyclonic regions ($x > 0$). The qualification of “broadly” is required because as discussed in section 4a, the separating eddies induce BBLs with opposite-signed vorticity on the downstream side of the seamount, so that a small amount of anticyclonic vorticity is generated in cyclonic regions ($x > 0$) and vice versa. Figure 11b highlights the result that for small values of Ro_L , the dissipation is predominantly in the anticyclonic region, in agreement with S19 and other studies.

However, as Ro_L increases, there is a symmetrization and a similar amount of dissipation occurs in the two regions implying (given the discussion in section 4c) that enhanced vertical shear induced parameterized mixing dominates at large Ro_L .

A more visual perspective on the symmetrization of ϵ is in Fig. 12, showing (x, y) sections of time-averaged energy dissipation for two values of $Ro_L = 0.1, 1$. When $Ro_L = 0.1$, ϵ is noticeably stronger for $x < 0$, i.e., the anticyclonic wake, and is largely limited to the region immediately downstream of separation. When $Ro_L = 1.0$, however, the strength of the dissipation is similar in both cyclonic and anticyclonic regions and encompasses the entire near wake. Concomitant snapshots of the gradient Richardson number $Ri_g = N^2/|\mathbf{v}_z|^2$ show widespread regions of small Ri_g when $Ro_L = 1$, which would trigger the Ri_g dependent mixing in the numerical model.

Previous theoretical and numerical studies have shown that the growth rate of the fastest growing centrifugally unstable mode has the approximate form $\sigma_{CI} \sim \sqrt{-f(\zeta + f)}$ (Hoskins and Bretherton 1972; Jiao and Dewar 2015), which is positive for finite f and $\zeta < -f$ (i.e., as is found in strong anticyclonic vorticity). Because the wake ζ is a weak function of f (Fig. 5), in the limit of $f \rightarrow 0$, the growth rate of the centrifugal instability in the anticyclonic wake should decay as \sqrt{f} . But, the prevalence of parameterized shear instabilities increases with decreasing f simply because the vertical shear increases (through Λ_h). Consequently, centrifugal instability is expected to dominate

in strong anticyclones when f is large (Ro_L is small), explaining the asymmetry in ε at small Ro_L , but for large Ro_L centrifugal instabilities do not manifest and shear instabilities should dominate; this causes symmetrization because the vertical shear generation has no relative preference between the cyclonic or anticyclonic regions.

c. Hydrostatic versus nonhydrostatic equations

ROMS solves the hydrostatic primitive equations and cannot accurately represent three-dimensional centrifugal and vertical shear instabilities (like KH instabilities) that often serve as a route to dissipation; this might be of particular relevance in the numerical simulations here that possess a strong forward energy cascade demonstrated in preceding sections. In our results, these three-dimensional instabilities are instead represented by parameterized vertical mixing, which is automatically triggered when Ri_g is small enough or in the presence of density overturns in the interior. One might be tempted to infer the need for solving the nonhydrostatic Boussinesq equations to capture the correct flow dynamics in the flow configurations studied here. However, it is important to note that merely solving the Boussinesq equations is insufficient; it is also critical that a sufficiently high horizontal resolution is employed in order to resolve the aforementioned three-dimensional instabilities, otherwise the Boussinesq model effectively solves the primitive equations. For example, Dewar et al. (2015) suggest using $\Delta x = 15$ m horizontal resolutions for resolving centrifugal instabilities. Because the model resolution here is $\Delta x \sim 300$ m, this represents a 20-fold increase in resolution along each dimension and a similar factor decrease in the time step due to CFL-number restrictions, thus a factor of $20^3 = 8000$ increase in computational cost. Nested modeling of the near-wake region can alleviate these concerns but only moderately. Instead we offer justification that the primitive equations combined with parameterized mixing might suffice for the phenomena simulated here.

Deusebio et al. (2013) compare numerical simulations of primitive equations with Boussinesq equations for the rotating-stratified turbulence transition problem at identical horizontal and vertical resolutions in a triply periodic domain. They find that in the limit of $f/N \rightarrow 0$, key flow properties like the energy spectrum and value of the eddy kinetic energy dissipation are similar in both classes of simulations, offering support for the sufficiency of primitive equations. A similar comparison in studying centrifugal instabilities by Dewar et al. (2015) and Jiao and Dewar (2015) demonstrates that the energy dissipation in Primitive and Boussinesq equations was of a similar order. We also conducted Boussinesq equation solutions at resolutions of up to $\Delta x = 35$ m (not shown) using nonhydrostatic ROMS (Roullet et al. 2017) with only marginal differences relative to the primitive equation solution, highlighting the need for even higher-resolution solutions in order to resolve the progression of the vertical shear instabilities.

6. Summary

In this study we examine the changes in the structure and dynamics of bottom-drag mediated vortical topographic wakes

as a function of the Coriolis parameter, f . We employ an idealized framework of a barotropic flow past a Gaussian seamount (half-width $L = 15$ km and height $h_s = 800$ m) in a uniform background stratification, $N = 6 \times 10^{-3} \text{ s}^{-1}$, and constant background f . Multiple numerical experiments using the Regional Ocean Model System (ROMS) are performed, each differing only by the background value of f that varies between values found in the latitudinal range 5° – 60° .

This study is motivated by realistic high-resolution ($\Delta x = 1.2$ km) ROMS simulations in the southwest Pacific that show a substantial increase in the vertical shear ($|\mathbf{v}_z| = \sqrt{u_z^2 + v_z^2}$) in topographic wakes equatorward of 10°S (Fig. 1; Srinivasan et al. 2017). Recent observations of topographic wakes around the Palau Archipelago in the north equatorial Pacific also find consistent values of high vertical shear (MacKinnon et al. 2019). High-wake vertical shear can trigger Kelvin–Helmholtz instabilities that lead to strong energy dissipation and mixing with consequences for water mass transformations. These expectations are consistent with recent observations in the Solomon Sea (Alberty et al. 2017) showing enhanced (non-tidal) mixing in and around the Solomon Sea where the current topographic interactions are strongest.

Our idealized experiments indeed show a monotonic increase in vertical shear in the wake with decreasing f (equivalently increasing $Ro_L = U/fL$) as seen in Fig. 4. Furthermore, the vertical structure of the wake displays a dramatic shift from vertically aligned (or columnar) and horizontally coherent $O(1) Ro_\zeta (\equiv \zeta/f)$ vortices [or submesoscale coherent vortices (SCVs)] when $Ro_L = 0.1$ to a wake consisting of highly layered sheets of vortices with horizontally large but vertically thin pancake vortices (as observed in stratified flows; Beckers et al. 2001) when $Ro_L = 1.0$. The aspect ratio of these eddies follows the scaling $L^1/H^1 \sim \sqrt{f/N}$ in the range $0.05 < Ro_L < 0.5$ but asymptotes to an f -independent value for cases with larger Ro_L values.

The far-wake, volume-integrated rms vorticity ζ^{rms} and vertical shear $\mathbf{v}_z^{\text{rms}}$ display very different dependencies on Ro_L : while ζ^{rms} increases only marginally, around 20% between $Ro_L = 0.05$ and $Ro_L = 1$, $\mathbf{v}_z^{\text{rms}}$ increases by a factor of 5 over the same range of Ro_L . This indicates that the vorticity and vertical shear are generated by different dynamical processes. An analysis of the integrated enstrophy (ζ^2) balance shows that vorticity is generated at the bottom on the slopes of the topography due to bottom drag, offering dynamical support for recent studies (Molemaker et al. 2015; S19). And the slope generation is only a weak function of Ro_L as expected from the far-wake ζ^{rms} . The dissipation of enstrophy is also localized near the topography itself, also showing weak variation with Ro_L .

The vertical shear generated at the bottom on the seamount slopes is, in contrast, due to advective processes in the near-wake interior; the bottom generation is negligible in comparison. This advective generation is maximum in the seamount near-wake ($y/L < 2$), and its peak value increases monotonically with Ro_L by a factor of 5 as Ro_L varies in the range $0.05 < Ro_L < 1.0$, mirroring the change in the far-wake $\mathbf{v}_z^{\text{rms}}$. We hypothesize that this advective generation engenders a turbulent forward cascade process, which is only partially resolved owing

to the fact that ROMS is a hydrostatic model. The dissipation of vertical shear variance, unlike that of the enstrophy, is nonlocal in the alongstream direction, with the dissipation term having nonzero values well downstream of the seamount (Fig. 10c). The EKE dissipation $\langle \varepsilon \rangle$ is a strong function of Ro_L unlike the EKE generation that displays only weak, nonmonotonic variations. The EKE dissipation is highly nonlocal, and its peak value monotonically increases with Ro_L . Furthermore, the alongstream position of the peak $\langle \varepsilon \rangle$ value also monotonically shifts downstream with increasing Ro_L . Given the similar functional and structural dependence of the vertical shear generation and the EKE dissipation on Ro_L (Figs. 9a and 10c) we infer that $\langle \varepsilon \rangle$ is likely caused by partially resolved Kelvin–Helmholtz instabilities in the interior.

The energy dissipation at small Ro_L is concentrated at the anticyclonic near-wake, but as Ro_L increases, it increases both in magnitude and downstream extent. Notably, the dissipation occurs almost symmetrically in the cyclonic and anticyclonic regions. This shift in the spatial structure of energy dissipation can be attributed as a centrifugal instability (which occurs preferentially in anticyclonic regions) to vertical shear driven (parameterized) KH instability (and other three-dimensional vertical shear instabilities) transition as Ro_L increases. The magnitude of the volume-integrated dissipation $\langle \varepsilon \rangle_V$ increases by an order of magnitude for $0.05 < Ro_L < 1$ reflecting that topographic wakes in the tropical regions have significantly stronger dissipation and, consequently, mixing. This has important implications in the Solomon Sea region (Fig. 1) that lies on key water mass transport pathways from the Pacific to the Indian Oceans (Mélet et al. 2011; Germineaud et al. 2016).

The phenomenon of topographic vorticity generation, boundary current separation, and interior wake instability is an important pathway to creating submesoscale currents with their forward energy cascade to diapycnal mixing and dissipation.

Acknowledgments. This work was funded by NASA Grant NNX13AP51G and used the Extreme Science and Engineering Discovery Environment (XSEDE) (Towns et al. 2014).

APPENDIX

The Mixing Terms $\langle \Lambda_{vmix} \rangle$ and $\langle \Omega_{vmix} \rangle$

The vertical shear mixing term, Λ_{vmix} takes the form

$$\Lambda_{vmix} = \langle u_z \partial_{zz} (vu_z) + v_z \partial_{zz} (vu_z) \rangle. \tag{A1}$$

Before applying the averaging, the first term can be expanded using the chain rule of derivatives as

$$u_z \partial_{zz} (vu_z) = \partial_z (v_z u_z^2) + vu_z u_{zzz}. \tag{A2}$$

Since there is no surface stress, $v_z|_{z=0} = 0$ while at the bottom, $v_z|_{z=-h_s} = -\kappa u^*$, which is just the log law of the wall (the same as that obtained from KPP). Then first only applying the z integral (remember that the $\langle \rangle$ operator involves x and z integrals and a t average) on this term, we get

$$\int_{-h_s}^0 u_z \partial_{zz} (vu_z) dz = \kappa u^* u_z^2|_{z=-h_s} + \int_{-h_s}^0 vu_z u_{zzz} dz. \tag{A3}$$

Thus,

$$\langle u_z \partial_{zz} (vu_z) \rangle = \frac{1}{T} \int_{t_0}^{T+t_0} \int_{-L_x/2}^{L_x/2} \kappa u^* u_z^2|_{z=-h_s} dx dt + \langle vu_z u_{zzz} \rangle, \tag{A4}$$

and similarly for the v term. Aggregating the u and v terms leads to (17). The vertical shear terms at the bottom are calculated using one-sided derivatives because they cannot directly be expressed in terms of the bottom shear τ_b as was possible for the vorticity (14).

The vertical enstrophy mixing term $\langle \Omega_{vmix} \rangle$ can be integrated by parts as

$$\begin{aligned} \langle \zeta \nabla \times \tau_z \cdot \hat{\mathbf{k}} \rangle &= \frac{1}{T} \int_{t_0}^{T+t_0} \int_{-L_x/2}^{L_x/2} \zeta_b (\nabla \times \tau)_b \cdot \mathbf{k} dx \\ &\quad - \langle \zeta_z \nabla \times \tau \rangle \cdot \hat{\mathbf{k}}. \end{aligned} \tag{A5}$$

The result in (14) follows on noting that

$$(\nabla \times \tau)_b = \tau_{z,b} \times \nabla h_b - \nabla \times \tau_b. \tag{A6}$$

REFERENCES

- Abernathey, R., and P. Cessi, 2014: Topographic enhancement of eddy efficiency in baroclinic equilibration. *J. Phys. Oceanogr.*, **44**, 2107–2126, <https://doi.org/10.1175/JPO-D-14-0014.1>.
- Alberly, M., J. Sprintall, J. MacKinnon, A. Ganachaud, S. Cravatte, G. Eldin, C. Germineaud, and A. Melet, 2017: Spatial patterns of mixing in the Solomon Sea. *J. Geophys. Res. Oceans*, **122**, 4021–4039, <https://doi.org/10.1002/2016JC012666>.
- Beckers, M., R. Verzicco, H. Clercx, and G. Van Heijst, 2001: Dynamics of pancake-like vortices in a stratified fluid: Experiments, model and numerical simulations. *J. Fluid Mech.*, **433**, 1–27, <https://doi.org/10.1017/S0022112001003482>.
- Billant, P., and J.-M. Chomaz, 2000: Experimental evidence for a new instability of a vertical columnar vortex pair in a strongly stratified fluid. *J. Fluid Mech.*, **418**, 167–188, <https://doi.org/10.1017/S0022112000001154>.
- Bischoff, T., and A. F. Thompson, 2014: Configuration of a southern ocean storm track. *J. Phys. Oceanogr.*, **44**, 3072–3078, <https://doi.org/10.1175/JPO-D-14-0062.1>.
- D’Asaro, E. A., 1988: Generation of submesoscale vortices: A new mechanism. *J. Geophys. Res.*, **93**, 6685–6693, <https://doi.org/10.1029/JC093iC06p06685>.
- Deloncle, A., P. Billant, and J.-M. Chomaz, 2008: Nonlinear evolution of the zigzag instability in stratified fluids: A shortcut on the route to dissipation. *J. Fluid Mech.*, **599**, 229–239, <https://doi.org/10.1017/S0022112007000109>.
- Deusebio, E., A. Vallgren, and E. Lindborg, 2013: The route to dissipation in strongly stratified and rotating flows. *J. Fluid Mech.*, **720**, 66–103, <https://doi.org/10.1017/jfm.2012.611>.
- Dewar, W., J. McWilliams, and M. Molemaker, 2015: Centrifugal instability and mixing in the California Undercurrent. *J. Phys. Oceanogr.*, **45**, 1224–1241, <https://doi.org/10.1175/JPO-D-13-0269.1>.
- Dong, C., J. C. McWilliams, and A. F. Schepetkin, 2007: Island wakes in deep water. *J. Phys. Oceanogr.*, **37**, 962–981, <https://doi.org/10.1175/JPO3047.1>.

- Epifanio, C., and D. Durran, 2002: Lee-vortex formation in free-slip stratified flow over ridges. Part II: Mechanisms of vorticity and PV production in nonlinear viscous wakes. *J. Atmos. Sci.*, **59**, 1166–1181, [https://doi.org/10.1175/1520-0469\(2002\)059<1166:LVFIFS>2.0.CO;2](https://doi.org/10.1175/1520-0469(2002)059<1166:LVFIFS>2.0.CO;2).
- Germeineaud, C., A. Ganachaud, J. Sprintall, S. Cravatte, G. Eldin, M. S. Alberty, and E. Privat, 2016: Pathways and water mass properties of the thermocline and intermediate waters in the Solomon Sea. *J. Phys. Oceanogr.*, **46**, 3031–3049, <https://doi.org/10.1175/JPO-D-16-0107.1>.
- Gill, A. E., 2016: *Atmosphere-Ocean Dynamics*. Elsevier, 682 pp.
- Gula, J., M. J. Molemaker, and J. C. McWilliams, 2015a: Topographic vorticity generation, submesoscale instability and vortex street formation in the Gulf Stream. *Geophys. Res. Lett.*, **42**, 4054–4062, <https://doi.org/10.1002/2015GL063731>.
- , —, and —, 2015b: Gulf Stream dynamics along the southeastern U.S. seaboard. *J. Phys. Oceanogr.*, **45**, 690–715, <https://doi.org/10.1175/JPO-D-14-0154.1>.
- , —, and —, 2016: Topographic generation of submesoscale centrifugal instability and energy dissipation. *Nat. Commun.*, **7**, 12811, <https://doi.org/10.1038/ncomms12811>.
- Harrison, D., and A. Robinson, 1978: Energy analysis of open regions of turbulent flows—Mean eddy energetics of a numerical ocean circulation experiment. *Dyn. Atmos. Oceans*, **2**, 185–211, [https://doi.org/10.1016/0377-0265\(78\)90009-X](https://doi.org/10.1016/0377-0265(78)90009-X).
- Hoskins, B. J., and F. P. Bretherton, 1972: Atmospheric frontogenesis models: Mathematical formulation and solution. *J. Atmos. Sci.*, **29**, 11–37, [https://doi.org/10.1175/1520-0469\(1972\)029<0011:AFMMFA>2.0.CO;2](https://doi.org/10.1175/1520-0469(1972)029<0011:AFMMFA>2.0.CO;2).
- Jagannathan, A., K. Srinivasan, J. C. McWilliams, J. M. Molemaker, and A. L. Stewart, 2021: Boundary layer-mediated vorticity generation in currents over sloping bathymetry. *J. Phys. Oceanogr.*, **51**, 1757–1778, <https://doi.org/10.1175/JPO-D-20-0253.1>.
- Jiao, Y., and W. Dewar, 2015: The energetics of centrifugal instability. *J. Phys. Oceanogr.*, **45**, 1554–1573, <https://doi.org/10.1175/JPO-D-14-0064.1>.
- Johnston, T. S., and Coauthors, 2019: Energy and momentum lost to wake eddies and lee waves generated by the north equatorial current and tidal flows at Peleliu, Palau. *Oceanography*, **32**, 110–125, <https://doi.org/10.5670/oceanog.2019.417>.
- Large, W., J. C. McWilliams, and S. C. Doney, 1994: Oceanic vertical mixing: A review and a model with a nonlocal boundary layer parameterization. *Rev. Geophys.*, **32**, 363–403, <https://doi.org/10.1029/94RG01872>.
- Lemarié, F., J. Kurian, A. F. Shchepetkin, M. J. Molemaker, F. Colas, and J. C. McWilliams, 2012: Are there inescapable issues prohibiting the use of terrain-following coordinates in climate models? *Ocean Modell.*, **42**, 57–79, <https://doi.org/10.1016/j.ocemod.2011.11.007>.
- Lilly, D. K., 1983: Stratified turbulence and the mesoscale variability of the atmosphere. *J. Atmos. Sci.*, **40**, 749–761, [https://doi.org/10.1175/1520-0469\(1983\)040<0749:STATMV>2.0.CO;2](https://doi.org/10.1175/1520-0469(1983)040<0749:STATMV>2.0.CO;2).
- MacKinnon, J. A., M. H. Alford, G. Voet, K. Zeiden, T. S. Johnston, M. Siegelman, S. Merrifield, and M. Merrifield, 2019: Eddy wake generation from broadband currents near Palau. *J. Geophys. Res. Oceans*, **124**, 4891–4903, <https://doi.org/10.1029/2019JC014945>.
- Marino, R., P. D. Mininni, D. Rosenberg, and A. Pouquet, 2013: Inverse cascades in rotating stratified turbulence: Fast growth of large scales. *Europhys. Lett.*, **102**, 44006, <https://doi.org/10.1209/0295-5075/102/44006>.
- Mason, E., M. J. Molemaker, A. Shchepetkin, F. Colas, J. C. McWilliams, and P. Sangrà, 2010: Procedures for offline grid nesting in regional ocean models. *Ocean Modell.*, **35**, 1–15, <https://doi.org/10.1016/j.ocemod.2010.05.007>.
- McWilliams, J. C., 1985: Submesoscale, coherent vortices in the ocean. *Rev. Geophys.*, **23**, 165–182, <https://doi.org/10.1029/RG023i002p00165>.
- , E. Huckle, and A. F. Shchepetkin, 2009: Effects in a stratified Ekman layer. *J. Phys. Oceanogr.*, **39**, 2581–2599, <https://doi.org/10.1175/2009JPO4130.1>.
- Mélet, A., J. Verron, L. Gourdeau, and A. Koch-Larrouy, 2011: Equatorward pathways of Solomon Sea water masses and their modifications. *J. Phys. Oceanogr.*, **41**, 810–826, <https://doi.org/10.1175/2010JPO4559.1>.
- Molemaker, M. J., J. C. McWilliams, and W. K. Dewar, 2015: Submesoscale instability and generation of mesoscale anticyclones near a separation of the California Undercurrent. *J. Phys. Oceanogr.*, **45**, 613–629, <https://doi.org/10.1175/JPO-D-13-0225.1>.
- Nikurashin, M., R. Ferrari, N. Grisouard, and K. Polzin, 2014: The impact of finite-amplitude bottom topography on internal wave generation in the Southern Ocean. *J. Phys. Oceanogr.*, **44**, 2938–2950, <https://doi.org/10.1175/JPO-D-13-0201.1>.
- Perfect, B., N. Kumar, and J. Riley, 2018: Vortex structures in the wake of an idealized seamount in rotating, stratified flow. *Geophys. Res. Lett.*, **45**, 9098–9105, <https://doi.org/10.1029/2018GL078703>.
- , —, and —, 2020a: Energetics of seamount wakes. Part I: Energy exchange. *J. Phys. Oceanogr.*, **50**, 1365–1382, <https://doi.org/10.1175/JPO-D-19-0105.1>.
- , —, and —, 2020b: Energetics of seamount wakes. Part II: Wave fluxes. *J. Phys. Oceanogr.*, **50**, 1383–1398, <https://doi.org/10.1175/JPO-D-19-0104.1>.
- Praud, O., J. Sommeria, and A. M. Fincham, 2006: Decaying grid turbulence in a rotating stratified fluid. *J. Fluid Mech.*, **547**, 389–412, <https://doi.org/10.1017/S0022112005007068>.
- Rosso, I., A. M. Hogg, P. G. Strutton, A. E. Kiss, R. Matear, A. Klocker, and E. van Sebille, 2014: Vertical transport in the ocean due to sub-mesoscale structures: Impacts in the Kerguelen region. *Ocean Modell.*, **80**, 10–23, <https://doi.org/10.1016/j.ocemod.2014.05.001>.
- Roulet, G., M. J. Molemaker, N. Ducouso, and T. Dubos, 2017: Compact symmetric Poisson equation discretization for non-hydrostatic sigma coordinates ocean model. *Ocean Modell.*, **118**, 107–117, <https://doi.org/10.1016/j.ocemod.2017.09.001>.
- Schär, C., 2002: Mesoscale mountains and the larger-scale atmospheric dynamics: A review. *Intl. Geophys.*, **83**, 29–42, [https://doi.org/10.1016/S0074-6142\(02\)80155-3](https://doi.org/10.1016/S0074-6142(02)80155-3).
- , and H. C. Davies, 1988: Quasi-geostrophic stratified flow over isolated finite amplitude topography. *Dyn. Atmos. Oceans*, **11**, 287–306, [https://doi.org/10.1016/0377-0265\(88\)90003-6](https://doi.org/10.1016/0377-0265(88)90003-6).
- Shchepetkin, A. F., and J. C. McWilliams, 2003: A method for computing horizontal pressure-gradient force in an oceanic model with a nonaligned vertical coordinate. *J. Geophys. Res.*, **108**, 3090, <https://doi.org/10.1029/2001JC001047>.
- , and —, 2005: The Regional Oceanic Modeling System (ROMS): A split-explicit, free-surface, topography-following-coordinate oceanic model. *Ocean Modell.*, **9**, 347–404, <https://doi.org/10.1016/j.ocemod.2004.08.002>.
- , and —, 2009: Correction and commentary for “Ocean forecasting in terrain-following coordinates: Formulation and skill assessment of the regional ocean modeling system” by Haidvogel et al., *J. Comp. Phys.* **277**, pp. 3595–3624. *J. Comput. Phys.*, **228**, 8985–9000, <https://doi.org/10.1016/j.jcp.2009.09.002>.
- Simmons, H. L., B. S. Powell, S. T. Merrifield, S. E. Zedler, and P. L. Colin, 2019: Dynamical downscaling. *Oceanography*, **32**, 84–91, <https://doi.org/10.5670/oceanog.2019.414>.

- Srinivasan, K., J. C. McWilliams, L. Renault, H. G. Hristova, J. Molemaker, and W. S. Kessler, 2017: Topographic and mixed layer submesoscale currents in the near-surface southwestern tropical Pacific. *J. Phys. Oceanogr.*, **47**, 1221–1242, <https://doi.org/10.1175/JPO-D-16-0216.1>.
- , —, M. J. Molemaker, and R. Barkan, 2019: Submesoscale vortical wakes in the lee of topography. *J. Phys. Oceanogr.*, **49**, 1949–1971, <https://doi.org/10.1175/JPO-D-18-0042.1>.
- St. Laurent, L., T. Ijichi, S. T. Merrifield, J. Shapiro, and H. L. Simmons, 2019: Turbulence and vorticity in the wake of Palau. *Oceanography*, **32**, 102–109, <https://doi.org/10.5670/oceanog.2019.416>.
- Towns, J., and Coauthors, 2014: Xsede: Accelerating scientific discovery. *Comput. Sci. Eng.*, **16**, 62–74, <https://doi.org/10.1109/MCSE.2014.80>.
- Vallgren, A., E. Deusebio, and E. Lindborg, 2011: Possible explanation of the atmospheric kinetic and potential energy spectra. *Phys. Rev. Lett.*, **107**, 268501, <https://doi.org/10.1103/PhysRevLett.107.268501>.
- Vic, C., G. Roullet, X. Capet, X. Carton, M. J. Molemaker, and J. Gula, 2015: Eddy-topography interactions and the fate of the Persian Gulf outflow. *J. Geophys. Res. Oceans*, **120**, 6700–6717, <https://doi.org/10.1002/2015JC011033>.
- Waite, M. L., and P. Bartello, 2006: The transition from geostrophic to stratified turbulence. *J. Fluid Mech.*, **568**, 89–108, <https://doi.org/10.1017/S0022112006002060>.
- , and P. K. Smolarkiewicz, 2008: Instability and breakdown of a vertical vortex pair in a strongly stratified fluid. *J. Fluid Mech.*, **606**, 239–273, <https://doi.org/10.1017/S0022112008001912>.
- Wijesekera, H. W., J. C. Wesson, D. W. Wang, W. J. Teague, and Z. Hallock, 2020: Observations of flow separation and mixing around the northern Palau island/ridge. *J. Phys. Oceanogr.*, **50**, 2529–2559, <https://doi.org/10.1175/JPO-D-19-0291.1>.
- Wright, C. J., R. B. Scott, P. Ailliot, and D. Furnival, 2014: Lee wave generation rates in the deep ocean. *Geophys. Res. Lett.*, **41**, 2434–2440, <https://doi.org/10.1002/2013GL059087>.
- Zhang, Z., Y. Zhang, B. Qiu, H. Sasaki, Z. Sun, X. Zhang, W. Zhao, and J. Tian, 2020: Spatiotemporal characteristics and generation mechanisms of submesoscale currents in the northeastern south china sea revealed by numerical simulations. *J. Geophys. Res. Oceans*, **125**, e2019JC015404, <https://doi.org/10.1029/2019JC015404>.